DALHOUSIE UNIVERSITY

STRUCTURE OF THE MOHOROVIČIĆ DISCONTINUITY (MOHO) AT THE EAST PACIFIC RISE FROM 3D MULTICHANNEL SEISMIC REFLECTION DATA

Graham Kerford

SUBMITTED IN PARTIAL FULFILLMENT OF THE REQUIREMENTS FOR
THE DEGREE OF BACHELOR OF SCIENCE, HONOURS
DEPARTMENT OF EARTH SCIENCE
DALHOUSIE UNIVERSITY, HALIFAX, NOVA SCOTIA

April 2018

Distribution License

DalSpace requires agreement to this non-exclusive distribution license before your item can appear on DalSpace.

NON-EXCLUSIVE DISTRIBUTION LICENSE

You (the author(s) or copyright owner) grant to Dalhousie University the non-exclusive right to reproduce and distribute your submission worldwide in any medium.

You agree that Dalhousie University may, without changing the content, reformat the submission for the purpose of preservation.

You also agree that Dalhousie University may keep more than one copy of this submission for purposes of security, back-up and preservation.

You agree that the submission is your original work, and that you have the right to grant the rights contained in this license. You also agree that your submission does not, to the best of your knowledge, infringe upon anyone's copyright.

If the submission contains material for which you do not hold copyright, you agree that you have obtained the unrestricted permission of the copyright owner to grant Dalhousie University the rights required by this license, and that such third-party owned material is clearly identified and acknowledged within the text or content of the submission.

If the submission is based upon work that has been sponsored or supported by an agency or organization other than Dalhousie University, you assert that you have fulfilled any right of review or other obligations required by such contract or agreement.

Dalhousie University will clearly identify your name(s) as the author(s) or owner(s) of the submission, and will not make any alteration to the content of the files that you have submitted.

If you have questions regarding this license please contact the repository manager at dalspace@dal.ca.

Grant the distribution license by signing and dating below.

_____ _____

Name of signatory Date

TABLE OF CONTENTS

List of Tables

List of Figures

ABSTRACT

The purpose of this thesis is to provide a detailed interpretation of the Mohorovičić discontinuity (MOHO) at the East Pacific Rise (EPR) using 3D multichannel seismic data collected between 9°37.5'N and 9°57'N in 2008. The MOHO was picked throughout the survey area extending for ~10 km on the western flank and ~12 km on the eastern flank of the ridge. Observations of the MOHO indicate that it is comprised of multiple terraces with single reflections closer to the ridge, becoming increasingly impulsive further away from the ridge. Low amplitude, off lapping reflections (OLRs) are observed to off lap from the outer edge of the terraces extending out over the deeper terraces. These OLRs extend over large swaths of the lower crust and have been interpreted as sills that are periodically injected from the upper mantle into the lower crust near the ridge axis. It is hypothesized that the sills are formed from magma that has built up at the MOHO due to an increase in lithostatic pressure. Later, when the lithostatic pressure is reduced, the magma is injected into the lower crust forming sills. Questions still remain regarding the formation and periodic nature of the terraces and the injection of sills into the lower crust. Seven terraces were observed on the eastern flank and 6 on the western flank of the ridge with a maximum crustal age of ~260 ka and 216 ka, respectively indicating that they both have a formation frequency of ~37 ka. This suggests that sea level changes associated with the 41 ka Milancović cycle may influence the timing of the formation of the terraces and sills.

Keywords: MOHO, East Pacific Rise, 3D Multi Channel Seismic Survey, terraces, off lapping reflections

LIST OF ABBREVIATIONS

Abbreviation	Name
AML	Axial Magma Lens
AMC	Axial Magma Chamber
CMP	Common Mid Point
EPR	East Pacific Rise
LVZ	Low Velocity Zone
MCS	Multichannel Seismic
MOR	Mid Ocean Ridge
OAML	Off-Axis Magma Lens
OLR	Off Lapping Reflection
TWT	Two-Way Traveltime

Acknowledgements

This honours thesis wouldn't have been possible without the valuable support, guidance, expertise and previous work completed by several people to whom I greatly appreciate.

Firstly, I would like to thank my supervisor Dr. Mladen R. Nedimović whom provided much needed guidance, expertise, and encouragement, especially in the early days of the thesis. He ensured that the project was conducted in a professional manner and understood the difficulties involved in geophysical interpretation, and was supportive throughout the extent of the project. Thank you very much for your patience, support and valuable insight in geophysics and tectonics in regards to my thesis.

A special thanks to my Co-Supervisor Dr. Matthew Salisbury for the continual support, and input into my thesis, and for reading my thesis. I would also like to thank you for your support and insights in relation to the findings of my thesis.

This thesis wouldn't have been possible without the dedication of Dr. Omid Aghaei who over a 6-year period processed all of the seismic data used for this thesis. I understand the huge amount of work required to process such a large dataset and express my sincere gratitude for the work that he put into this project.

I would also like to thank Masoud Aali and John Thibodeau for their assistance with the technical issues I encountered in the lab.

Thank you Dr. Djordje Grujic, for reviewing and acting as an examiner for this dissertation.

1.0 INTRODUCTION

1.1 Oceanic Crust

Oceanic crust covers almost 60% of the Earth's surface and is continuously being formed at mid ocean ridges (MORs). Although the oceanic crust is extremely widespread, it is challenging to study its formation, structure and composition due to its inaccessibility. MORs provide a vital insight into plate tectonics and into the processes involved in the accretion of oceanic crust.

Over the past 60 years, extensive research has been conducted using seismology to identify the layers present in the oceanic crust. Initial seismic studies indicated that the oceanic crust is composed of two homogenous layers of igneous rock, layer 2 and layer 3 with average compressional wave velocities of <6 km/s and 6.3-7.2 km/s, respectively [*Christensen and Salisbury, 1975*]. Further studies subdivided layer 2 into layers 2A and 2B (Figure 1) [*Houtz and Ewing,* 1976]. Using synthetic modeling and data from ocean bottom seismometers, a structural model with layers of varying velocity gradients replaced the homogenous layers model [*Spudich and Orcutt,* 1980]. In this model, a rapid increase in the velocity of seismic waves is observed in layer 2 followed by a gradual increase in layer 3 [*Orcutt and Kennett*, 1975]. The MOHO transition zone is observed at the base of layer 3 and is characterised by a rapid increase in the velocity of seismic waves. Comparison of ophiolites and laboratory measurements of dredge and core samples was used to interpret the seismic velocities observed in the oceanic crust and to identify the lithology of the crust *[Spudich and Orcutt, 1980]*. Using these methods, the following generic lithological model of the oceanic crust was produced: Top layer 2A has low P-wave velocities of ≥2.5 km/s and consists of pillow lavas that are underlain by sheeted dykes forming layer 2B with P-wave velocities between 5.5 – 6.0 km/s. P wave velocities indicate that layer 3 is composed of gabbroic mafic rocks with P-wave velocities of ~6.8 km/s [*Karson,* 1998].

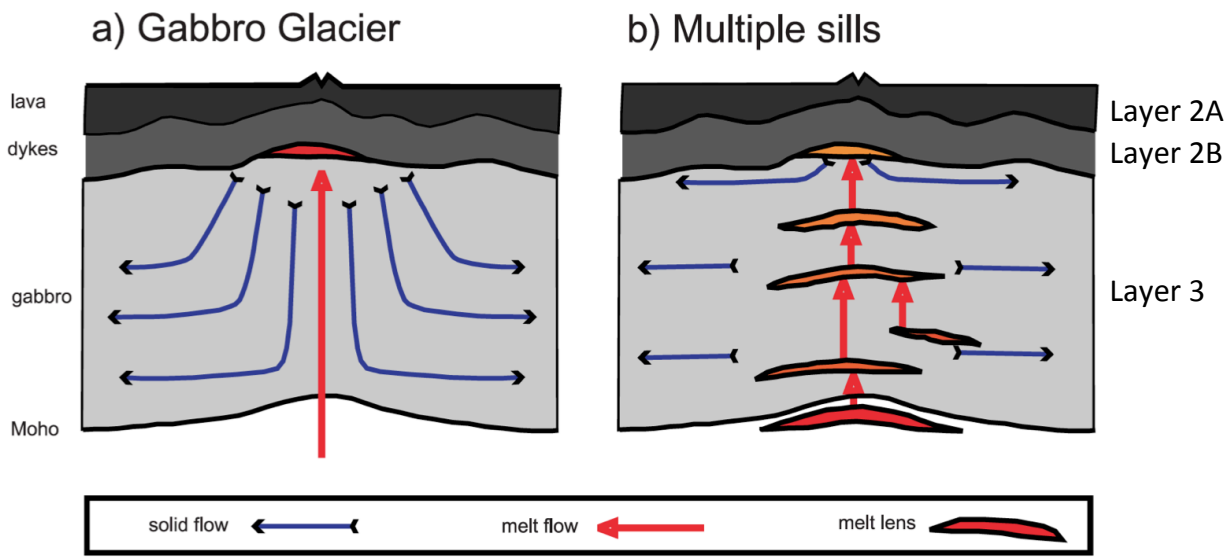

Figure 1.1 Crustal accretion models redrawn from *Korenaga and Kelemen* [1998]. (a) Gabbro glacier model where the lower crust is formed from the gravitational settling of material from the axial magma lens. (b) Multiple sills (sheeted-sills) model where the lower crust is formed in-situ from multiple sills. Figure from *MacLennan et al.* [2004].

1.2 Crustal Accretion

Studies in the 1970s suggested the presence of a large magma chamber at the base of the upper crust to explain the structural layering observed in ophiolites. The magma chamber was theorized to have an average width of about 8 km and would undergo differentiation and convection during crystallization [*Cann,* 1974]. This model explained the different layers observed in the crust with intrusions leading to the formation of layer 3 in the lower crust, and eruptions producing the vertical dikes of layer 2B and extrusives of layer 2A, such as pillow lavas, leading to the formation of the upper crust. Crystallization along the margins of the chamber would produce a thick layer of isotropic gabbro in the upper section of layer 3, while accumulation at the base of the chamber would produce layers of gabbro and ultramafics in the lower section of layer 3 [*Sinton and Detrick*, 1992].

To test this theory a 2D multichannel seismic (MCS) survey was conducted over the East Pacific Rise (EPR) between 8°30'N and 10°N. This survey identified a bright mid-crustal seismic reflection that was identified as the top of the axial magma chamber, and a low velocity zone (LVZ) below the axis of the MOR *[Herron et al., 1980]*. Further 2D MCS surveys and tomography

surveys over the EPR have identified the presence of a thin (<100 m thick) axial magma lens (AML) only 0.25-4 km wide in the upper crust at a depth of 1.4-1.75 km (Figure 1.2), rather than a thick 8 km wide magma chamber [*Detrick et al*., 1987, *Kent et al.,* 1993]. The AML is underlain by a 5-7 km thick partially molten zone characterized by a LVZ [*Toomey et al.,* 1990; *Vera et al.,* 1990] resulting in a significant shift in the understanding of MORs.

Similar studies conducted over slow and intermediate-spreading ridges have indicated that not all MORs have a visible AML or LVZ. 2D MCS surveys conducted over the Mid-Atlantic-Ridge (MAR) have shown that a significant amount of the ridge is devoid of an AML [*Derrick et al., 1990*]. Probably because of a higher rate of magma supply, an AML has been identified just south of the Kane Fracture zone at 23°15'N, one of the most hydrothermally active areas of the ridge [*Calvert, 1995*]. However, the rough bathymetry of the slow spreading mid Atlantic ridge is likely impacting the imaging process and our ability to identify AML reflections.

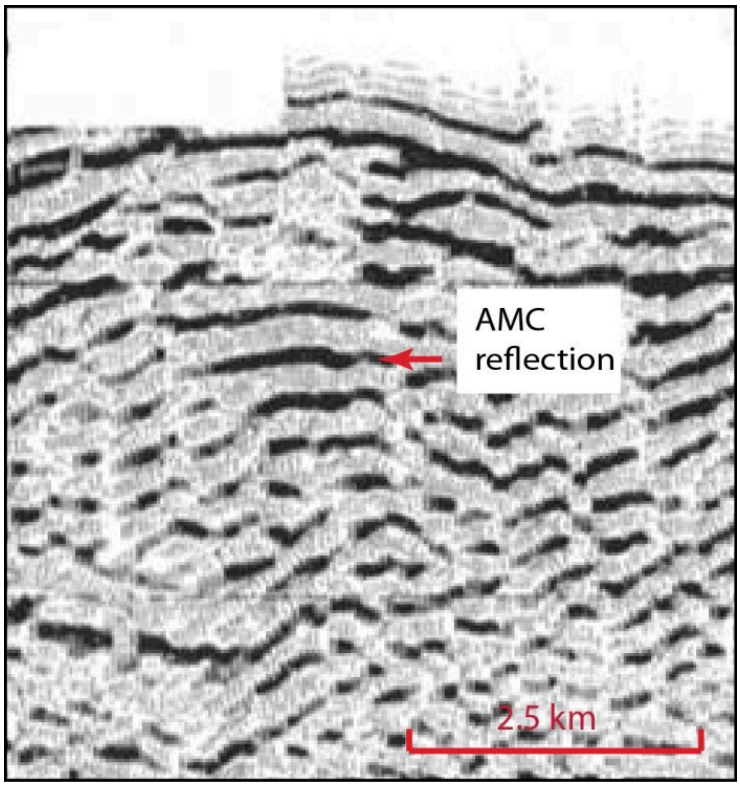

Figure 1.2 Multichannel seismic reflection image across the East Pacific Rise displaying an event interpreted as an axial magma lens. Adapted from *Heron et al.* [1980]. (From *Aghaei, PhD. thesis,* 2013 and references therein).

Two models of crustal accretion have been proposed using data collected from structural studies of ophiolites based on the presence of the AML. The gabbro-glacier model (Figure 1.1a), the simpler of the two models, indicates that the lower oceanic crust is formed from partial crystallization of the AML followed by a downward ductile flow [*Chen and Phipps Morgan, 1996*]. The second model, proposed by Shouten and Denham *[1995]*, places two AMLs in the lower crust, one at the base layer 2B and the second at the MOHO. Unlike the gabbro glacier model, the dual-sill model attempted to explain the petrological differences observed between the lower layered unit and upper gabbro units of the Oman ophiolite [*Boudier et al., 1996*]. The dual-sill model, however, requires 50% of the oceanic crust to be crystallized at the base of the crust, necessitating a significant amount of hydrothermal convection and thermal conduction to cool the magma [*Kelemen and Aharanov, 1998*]. For this reason the dual-sill model has since been refined into the multiple sill model (Figure 1.1b). In this model, the lower crust is formed from multiple sills placed between the base of the crust and layer 2B [*Kelemen and Aharanov, 1998*].

Structural mapping of the Oman ophiolite has led to a suggestion that mantle diapirs ~10km across feed the upper mantle at a frequency of once in ~70 years [*Boudier and Nicolas, 2011*; *Toomey et al., 2007*]. At the limits of the diapir the MOHO transition zone is thinned to less than 100 m with a maximum thickness of 300 m away from the diapir [*Jousselin and Nicolas, 2000*]. In order for the mantle to supply the AML with enough magma to ensure the continuous accretion of new crust, it is possible that magma percolates up through the lower crust [*Nicolas and Boudier, 2015*] forming the LVZ below the AML.

1.3 MOHO Structure

At the EPR the MOHO is displayed as a prominent reflection at roughly 2 s crustal two-way traveltime (TWT) [*Barth and Mutter, 1996*]. Seismic modelling of the MOHO has shown that it is better characterized as a transition zone (MOHO) of varying thickness rather than as a single discontinuity [*Vera et al., 1990*]. The MOHO reflections are characterized by 3 different

reflection responses: impulsive, shingled, and diffusive [*Kent et al., 1994*] (Figure 1.3). The impulsive and shingled reflections are associated with a thin MOHO transition zone (MOHO) [*Nedimović et al., 2005*] and are characterized by a single-phase event. Impulsive reflections differ from shingled reflections in that they are laterally continuous while shingled MOHO is composed of multiple smaller sections that are vertically offset from one-another. Diffusive MOHO is identified as a multi-phase event and is associated with a thicker MOHO [*Nedimović et al., 2005*].

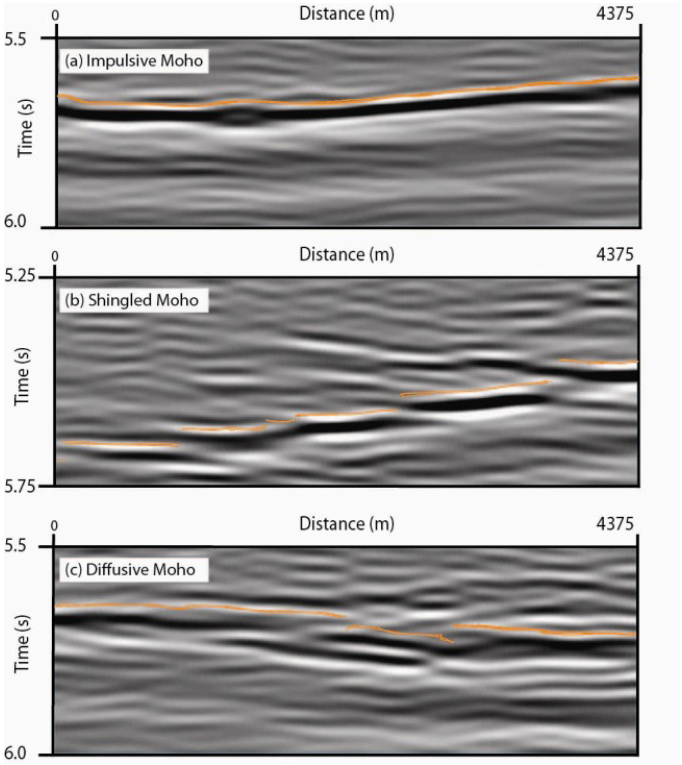

Figure 1.3 Close up images of the different types of MOHO reflections observed in the study area: (a) impulsive; (b) shingled; (c) diffusive. The orange line represents the picked horizon of the MOHO transition zone. (From *Aghaei et al., 2014* and references therein).

In 2008 the first high-resolution 3D MCS survey conducted over a spreading center was completed above the EPR. The survey was a collaborative effort between Lamont-Doherty Earth Observatory, Woods Hole Oceanographic Institute, and Dalhousie University. Interpretation of the migrated stack 3D image volume resulted in identification of the reflection MOHO below ~87% of the study area [*Aghaei et al., 2014*]. Typically the MOHO wasn't visualized below the AMLs and the off-axis melt lenses (OAMLs). Subsequent interpretation on a 3D prestack time migrated image volume, also by Aghaei et al [*2014*] identified MOHO reflections throughout

92% of the study area with 37% of the MOHO reflections being impulsive, 25% shingled (also impulsive but divided in segments ≤2 km in length), and 28% diffusive. Many of the newly identified Moho reflections originate from the axial region and/or from under the OAMLs.

Between 9° 48’ N and 9° 50’ N, Aghaei et al [*2014*] observe that the MOHO reflections change from impulsive single phased reflections to shingled reflections with small vertical offsets but did not investigate their continuity or symmetry across the ridge. The MOHO picks had a high to medium uncertainty in the southern study area and in the northern half of the northern study area. Within these areas the MOHO was interpreted as either diffusive or shingled MOHO. In the southern half of the northern area the MOHO had a low uncertainty of picking and was primarily identified as impulsive (Figure 1.4).

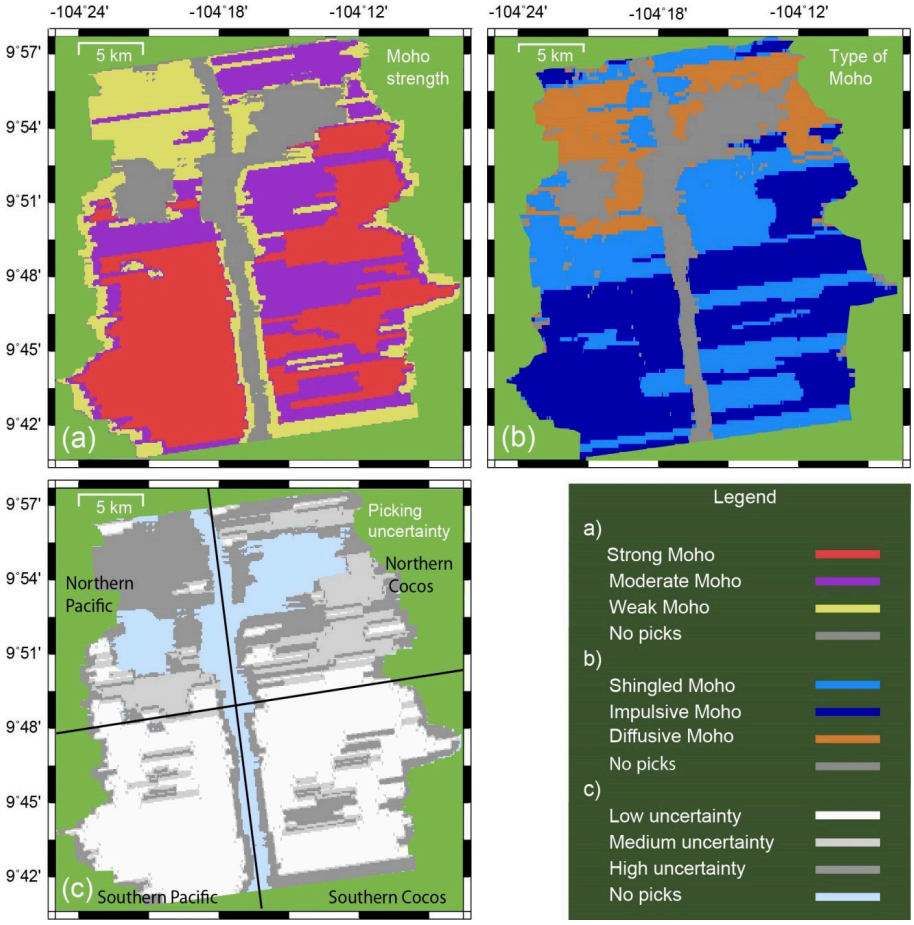

Figure 1.4 Map of the characteristics of the MOHO transition zone: (a) Strength of MOHO reflections; (b) type of MOHO reflection; (c) picking uncertainty. These maps were produced analysing the in-lines and cross-lines of the larger northern 3D survey area at 300 m and 150 m intervals, respectively. (From Aghaei et al., 2014).

1.4 Objective

Over the past half-century seismic studies over the MORs have significantly improved our understanding of the structure and processes involved in the formation of oceanic crust. However, most of the MOR studies have been sparse 2D MCS surveys that provide little knowledge regarding the geometry and continuity of oceanic crustal structures, especially of the deeper structures that are more challenging to image. The first true 3D MCS survey conducted over the EPR completely changes this by allowing for a detailed analysis of the structure of the MOHO, which is yet to be fully conducted. My goal and contribution to this quest is careful picking of the MOHO and nearby reflections using the 3D prestack time migrated reflection volume produced by Aghaei et al [*2014*], followed by a detailed interpretation of the identified structures.

2.0 STUDY AREA

The study area examined here is located over a 37 km long section of the EPR in the Pacific Ocean approximately 890 km SW of Mexico between 9°37.5'N and 9°57'N, with the Cocos plate to the east and the Pacific plate to the west (Figure 2.1). The MOR within the study area has an average spreading rate of 11 cm/yr (full rate) that has been relatively constant over the past ~730 Ka [*Carbotte and Macdonald, 1992*]. The survey extends ~14 km to the east and ~12 km to the west on either side of the ridge, with crustal ages up to ~260 Ka and 216 Ka, respectively, assuming a half spreading rate of 5.5 cm/yr.

Figure 2.1 Overview of the tectonic plates with the location of the survey area shown by the red star (From Nchsbands.info, 2017).

The study area is within a segment of the ridge which is a second order spreading center bounded to the north at ~10°10'N by the Clipperton transform fault and to the south at ~9°03'N by an overlapping spreading center, with a total offset of 85 km and 8 km, respectively (Figure 2.2) [*Macdonald et al., 1992*]. The study area is the most investigated area of the MOR system and has been subjected to extensive geophysical, geological, geochemical, geomorphic and hydrothermal studies [*Aghaei et al., 2014*].

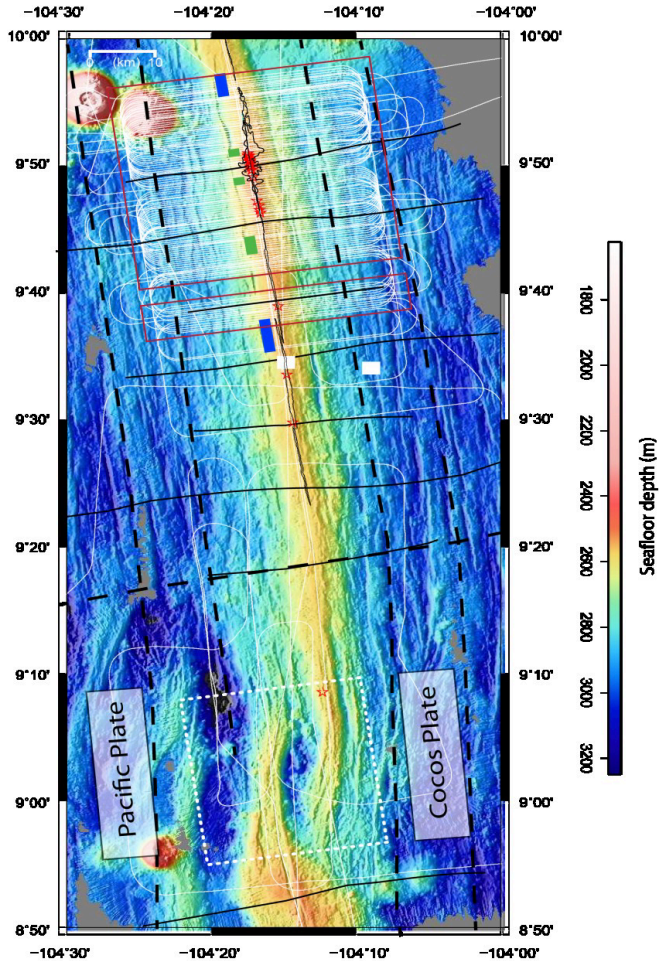

Figure 2.2 Ships tracks for the MGL0812 cruise shown in white overlay bathymetry data collected over the East Pacific Rise. (From *Aghaei, PhD. thesis,* 2013 and references therein).

Previous 2D MCS surveys have identified the presence of a 0.5-1.2 km wide AML extending from the OSC at 9 03'N to the Clipperton fault in the north indicating that the study area is part of an active magmatic system. The AML was located at a depth of 1.4-1.9 km below the seafloor with an average thickness of 10-50 m [*Kent et al., 1993*]. Extensive OAMLs have been identified in the mid and lower crust, with mid-crustal ones being much larger and occurring only on the Cocos plate [*Aghaei et al., 2014*]. The OAMLs, as described by *Canales et al.* [2012], typically occur between 5.5 km-7 km from the axis of the ridge and vary from 2.1 km-4.2 km below the seafloor. The MOHO reflections have been interpreted at a depth of 2 s TWT [*Herron et al., 1980*], with reflections being identified no closer than 2-3 km from the ridge axis [*Detrick et al., 1987*]. More recent surveys conducted within the study area (Figure 2.3) [*Aghaei et al., 2014*]

and over the OSC by Singh et al. [*2006*] have been able to image the MOHO beneath the crest of the MOR.

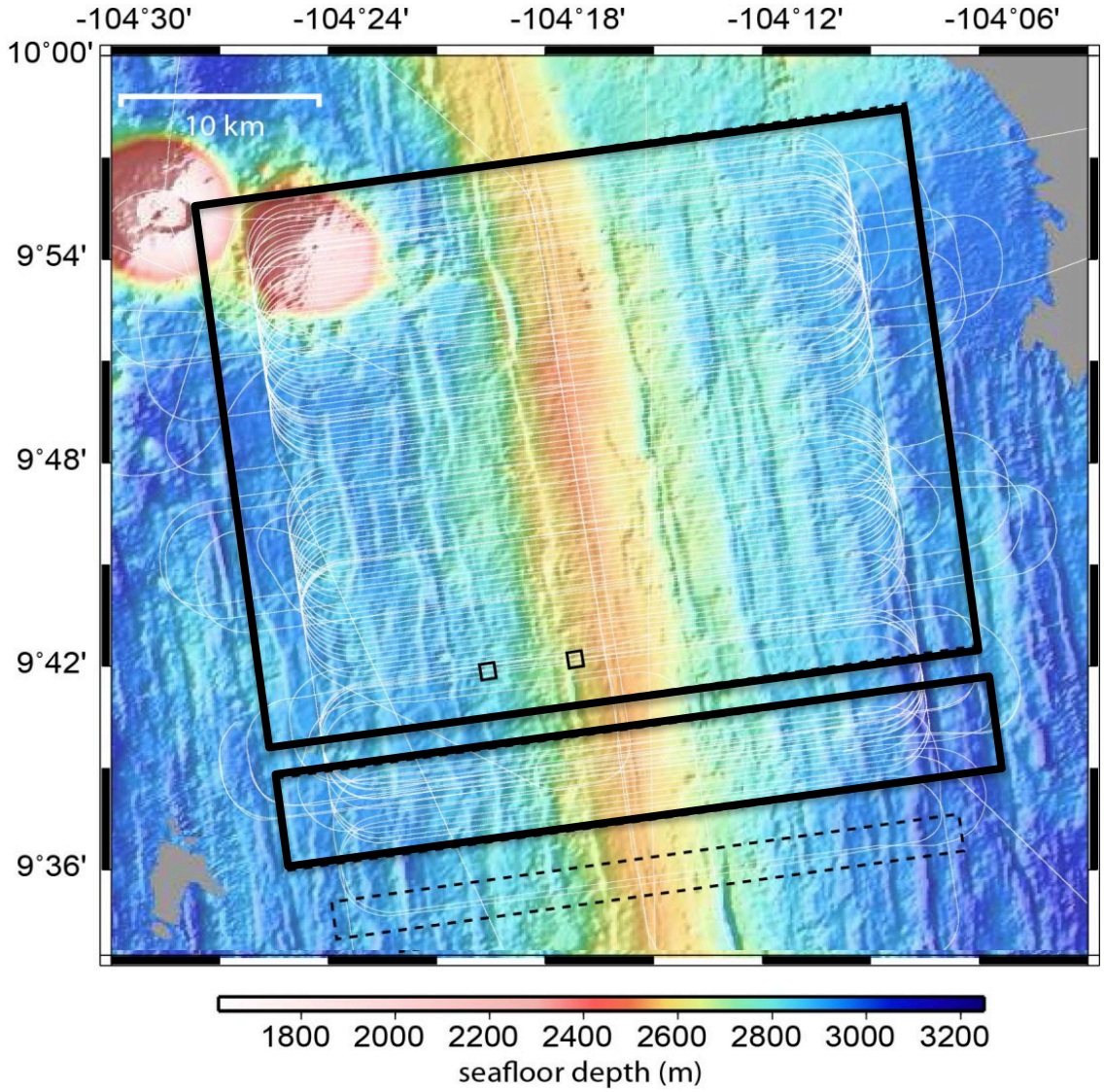

Figure 2.3 Ship track for cruise MGL0812 is shown using white lines, overlying a bathymetric grid between 9˚36'N and 10˚N latitude. Survey areas outlined in black. The youngest Lamont Seamount is shown in the NW section of the northern survey area (From Aghaei, 2013 and references therein).

3.0 DATA

3.1 Data Acquisition

In 2008 a 3D MCS survey was conducted onboard the R/V Marcus Langseth during the MGL0812 expedition. Four 6 km long hydrophone streamers with 150 m spacing were towed at a depth of 10 m with a total spacing of 450 m. Each streamer was composed of 468 receiver-array groups

spaced every 12.5 m with a total recording time of 10240 ms and a sample rate of 2 ms. Two seismic sources, each composed of two linear arrays of nine air guns were positioned at a depth of 7.5 m and were fired every 37.5 m in an alternating mode. This resulted in eight CMP profiles per sail line (inline) each separated by 37.5 m. Each sail line was 24 km long and they were separated by 300 m, providing 16 km of full-fold coverage. Each CMP bin is 37.5 m wide (cross ridge axis) and 6.25 m long (along-ridge-axis) [*Aghaei et al., 2014*]. To ensure accurate positioning of each airgun and streamer, the Global Positioning System, acoustic transponders and streamer compasses were used, with an accuracy of 1 m and <3 m, respectively [*Aghaei et al., 2014*].

The survey area is comprised of two survey blocks separated by a 3.3 km gap. The northern area is located between 9°42'N and 9°57'N with a total area ~714 km^2 and is comprised of 94 sail lines. The southern, smaller area, is comprised of 14 sail lines and is located between 9°37.5'N and 9°40'N with a total area of ~100km^2 [*Aghaei et al., 2014*]. For a more detailed assessment of the data acquisition, see *Aghaei et al.,* [2014].

3.2 Data Processing

The data was processed by *Aghaei et al [2014]* using bandpass filtering, geometric spreading correction, amplitude balancing, deconvolution, velocity analysis and stacking, and 3D Kirchoff migration. The data were also 3D prestack time migrated using the Kirchhoff approach. This latter approach yielded the best results that were used for this work after very minor cosmetic processing to reduce the noise and amplify the MOHO reflections. This final preparation of the 3D prestack time migrated data is described here. The number of Inlines and X-lines for both survey blocks had to be specified to upload the data correctly (Table 3.1). Once uploaded into Petrel, a time gain and an Ormsby filter (Bandpass filter) with a cosine taper were applied to each survey area (Tables 3.2 & 3.3).

Table 3.1 Number of X-lines and Inlines for each Seismic Survey Area in Petrel

	Northern Area	Southern Area
# of Inlines	189	20
# of X-lines	193	181

Table 3.2 Time gain Applied to each Seismic Cube for both Survey Areas ($Amp = Amp_{old} * t^n$, n = integer)

	Northern Area	Southern Area
Integer	4	0.5

Table 3.3 Parameters for the Ormsby Bandpass Filter in Petrel for the Northern and Southern Survey Area.

Start (ms)	End (ms)	Taper (ms)	Lf Pass (Hz)	Lf Cut (Hz)	Hf Pass (Hz)	Hf Cut (Hz)
0	-4750	250	10	20	40	50
-4750	-6500	250	5	10	20	30

3.3 Reflection Horizon Picking

The seismic reflections were interpreted as horizons in Petrel along the inlines and were picked at the crossing between the negative (white) and positive (black) amplitude responses belonging to the same reflection event (base of negative, top of positive amplitude responses). A "horizon" refers to the picked surface representing each reflection event. The picking parameters for the horizons are shown in Table 3.4. In areas where there was significant uncertainty regarding the location of the MOHO, the X-lines were used as an aid for interpretation; however, due to their much greater spacing, no extensive interpretation was conducted using the X-lines.

Table 3.4 Parameters used to pick the Horizons for the MOHO Reflections

	Picking Parameters
General Parameter	Returns between 5-6 seconds in two-way time Non-repetitive (not a multiple) Negative amplitude is the first response of the reflector (thus not a magma lens) Horizon can be traced over 3 inlines (>100 m) Minimum amplitude of 5E+7 (1E+8 to -2E+8 scale) **OR** Anticlinal shape

3.3.1 MOHO Reflections

The MOHO reflections are classified as the primary reflections observed at the MOR with the highest amplitude responses. In Petrel, these responses were characterized as being in the upper half of the amplitude scale (>5.0E+7 in a 1.0E+8 to -2.0E+8 scale). Each reflection was

interpreted as an individual horizon (Figure 3.1) allowing overlapping reflections to be fully picked.

If two horizons merged together, the larger horizon would be dominant over the smaller horizon and would be used to interpret the newly merged reflection. The larger horizon was chosen to be dominant because it resembled the newly formed horizon the best, resulting in less fluctuation in the interpretation of the horizons. The exception to this rule is the horizon closest to the ridge axis. Reflections on either side of the ridge, for this horizon, were interpreted as the same horizon because some reflections were picked as a single continuous horizon across the ridge axis. Since individual seismic horizons can be followed over long distances parallel to the ridge axis on the X-lines they were grouped together and numbered as individual terraces based on their depths. A terrace was defined as a vertical break of >50 ms between two horizons and picked horizons were classified based on what terrace they are associated with. As presented in Figure 3.1, the reflections tend to overlap downslope like roof shingles.

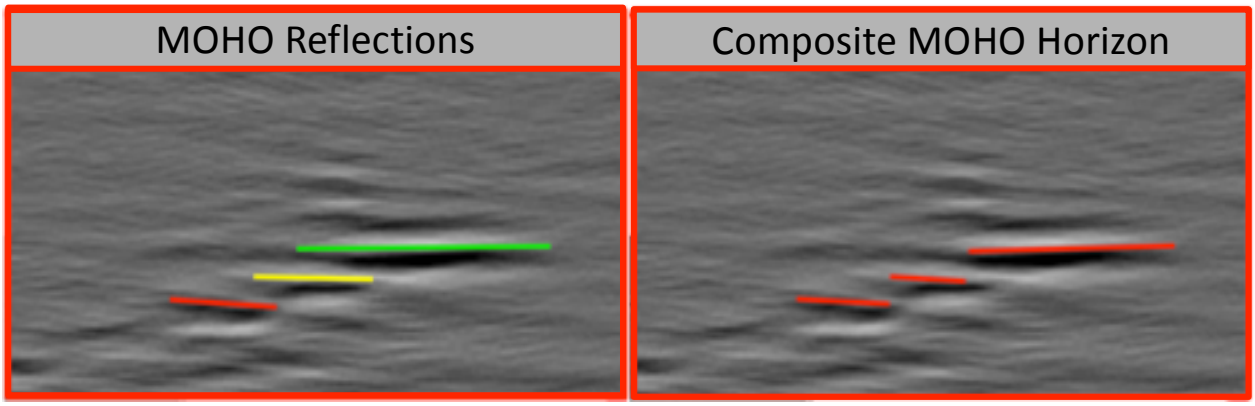

Figure 3.1 Picking variations between the interpretation of the MOHO reflections (a) and the simpler composite MOHO horizon (b). In the MOHO reflections interpretation each horizon was picked individually while all of the reflections were collectively interpreted as a single horizon with no overlap in the composite MOHO horizon interpretation.

3.3.2 Composite MOHO Horizon

To display the overall structure of the MOHO more clearly, the MOHO reflections were also mapped as a single composite MOHO horizon without any overlap. When interpreting the

MOHO reflections, each horizon was interpreted individually producing vertical gaps between each of the reflections. If two reflections overlaped, the section along both reflections with the highest amplitude of either reflection was picked.

3.3.3 Off Lapping Reflections (OLRs)

Weak reflections were observed above the main MOHO reflections and appear to be off lapping from the MOHO reflections. These reflections were picked with the same picking parameters as the MOHO reflections in Table 3.5, but using a lower amplitude limit >1.25E+7 in a 1.0E+8 to -2.0E+8 colour scale. The OLRs were picked independently following the same protocols used for picking the MOHO reflections. This provides us with the extent of the OLRs throughout the survey area.

4.0 RESULTS

The MOHO was identified throughout most of the study area. Areas where MOHO was not picked below the AML are between 1096000 mN and 1084800 mN, and 1082200 mN and 1072000 mN. The MOHO was not picked below the youngest Lamont Seamount in the NW section of the block (9°53’49N & 104°12’34W) and below some of the OAMLs (Figure 2.3 & 4.1). The uncertainty of the picking of the horizons differed greatly throughout the study area but follows a similar trend to the Aghaei et al [*2014*] interpretation (Figure 1.4). The greatest uncertainties are in the northern half of the northern survey area and eastern ridge flank of the southern survey area. These uncertainties are due to a decrease in resolving power of the imaging method caused by large lateral variations is seismic velocity generated by increased magmatism and structural complexity at the northern and southern ends of the data cube.

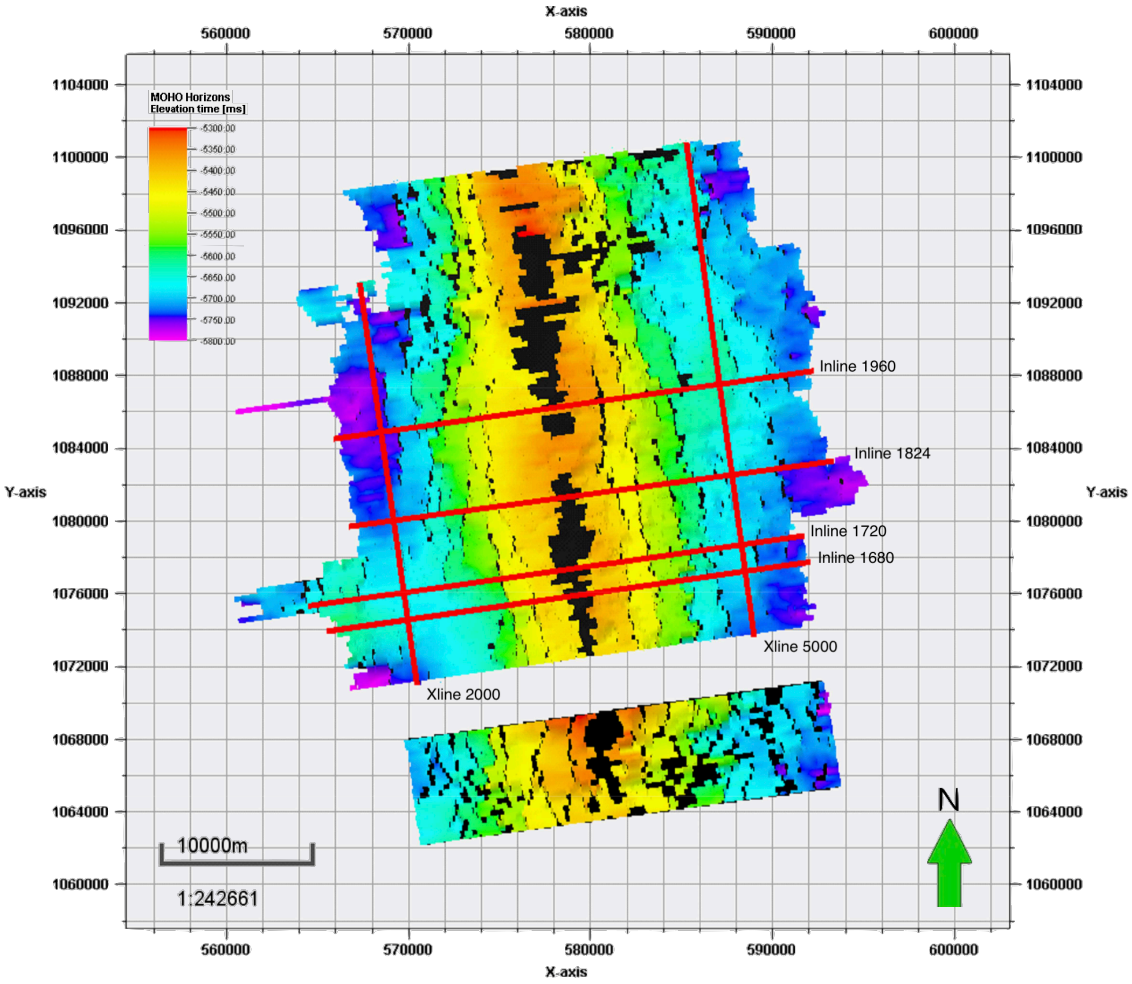

Figure 4.1 Overview of both survey blocks. Both axes are distance in meters with original latitudes and longitudes converted to UTM using geodetic reference frame WGS84 and zone 13N. Depths in ms TWT indicated by colour scale; black background used to increase contrast. Seismic Xlines and Inlines displayed in this section are shown in red.

4.1 MOHO Reflections

The MOHO in the study area (Figure 4.1) has an antiformal shape similar to the bathymetric expression of the EPR (Figure 2.2). The ridge is more steeply dipping along the western ridge flank with the steepest dip just to the west of the axis (Figures 4.2a & 4.2b). Parallel to the ridge axis, the MOHO is mostly flat with a nearly continuous reflection along the edges of the northern cube (Figures 4.3a & 4.3b). Due to OAMLs, it was not possible to pick the MOHO at the northern section of the northern survey area. On the western ridge flank, the MOHO is divided into multiple segments that onlap one-another, with the southern segments onlapping the

northern segments (Figure 4.4). Throughout the survey area extensive sub-MOHO reflections were observed, but time constraints prevented their interpretation (Figures 4.2 & 4.3).

The MOHO is composed of 6-7 nearly horizontal, shallow dipping terraces that, to a first approximation, are symmetrically disposed across the ridge axis and dip away from the axis like roof shingles (Figure 4.2a). In general, the terraces are about <2 km wide and extend for long distances, as much as 40 km, parallel to the axis of the ridge (Figure 4.2 & 4,3). The western terraces tend to be show more complicated geometry and overlap more extensively but most terraces are dominated by 1 or 2 horizons and some either merge with or split into multiple smaller terraces (Figures 4.4 & 4.5). MOHO couldn't be imaged along the majority of the ridge axis because of high P-wave attenuation below the AML and other imaging challenges such as large lateral velocity variations. In some areas it was possible to distinguish low amplitude anticlinal reflections that conformed to the top terrace on one or both sides of the ridge axis. These low-amplitude reflections were interpreted as Off Lapping Reflections (OLRs), however more detailed analyses would be required to confirm this interpretation.

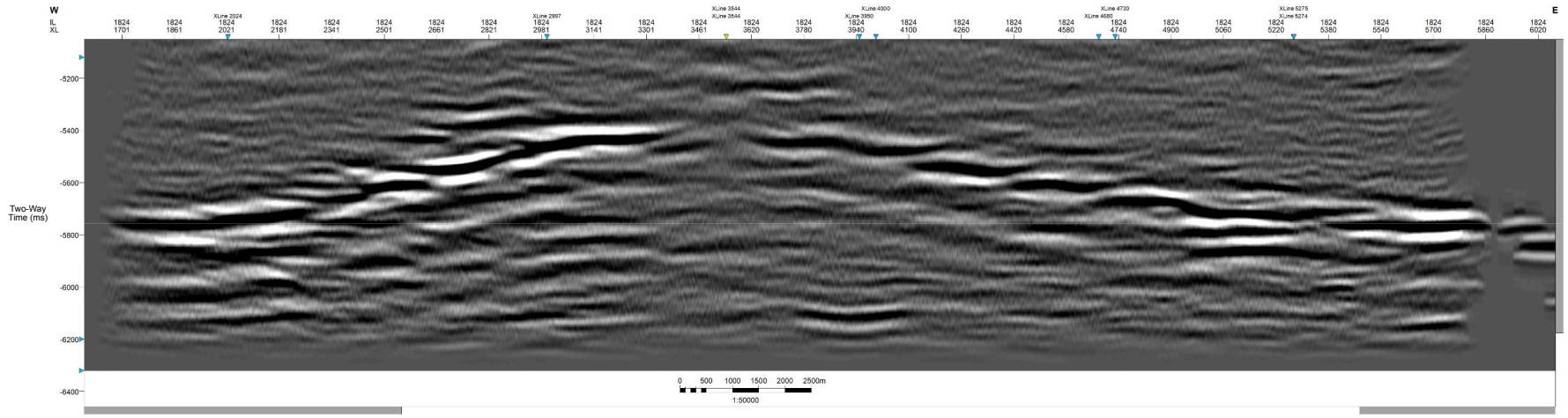

Figure 4.2a Inline 1824 located at the mid-southern section of the northern survey area. Two-way time is displayed in ms. Vertical exaggeration of ~1.7 assuming a lower crustal velocity of 6000 m/s. The western side of the ridge has a significantly steeper dip than the eastern side.

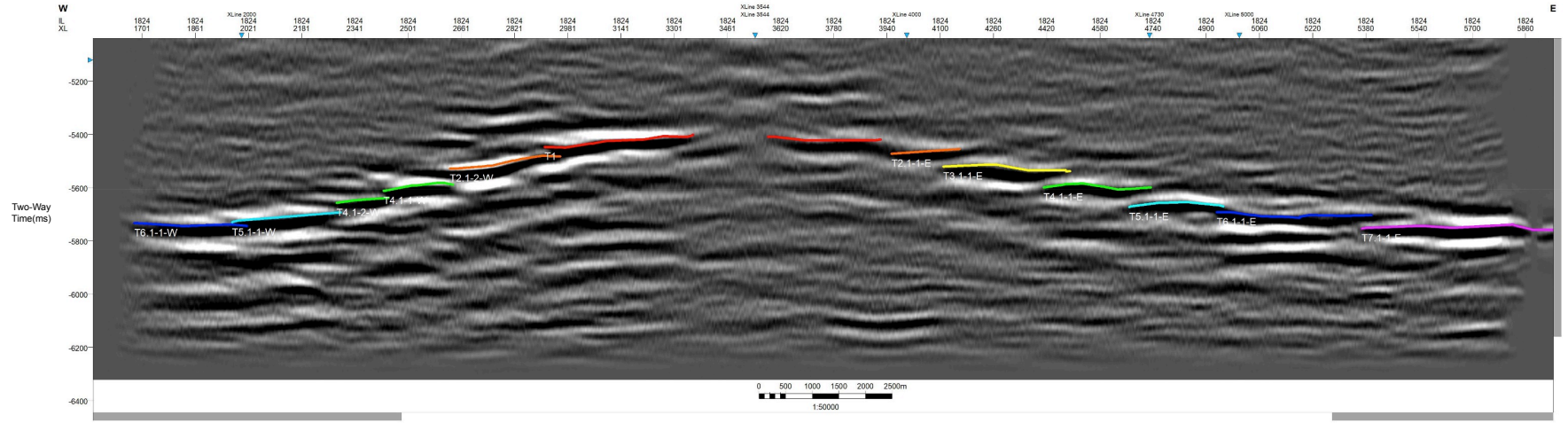

Figure 4.2b Inline 1824 located on the mid-southern section of the northern survey area. Two-way time displayed is in ms. Vertical exaggeration of ~1.7 assuming a lower crustal velocity of 6000 m/s. MOHO reflection picks are displayed using different colors to distinguish each terrace: 1 red, 2 orange, 3 yellow, 4 green, 5 cyan, 6 blue, and 7 pink.

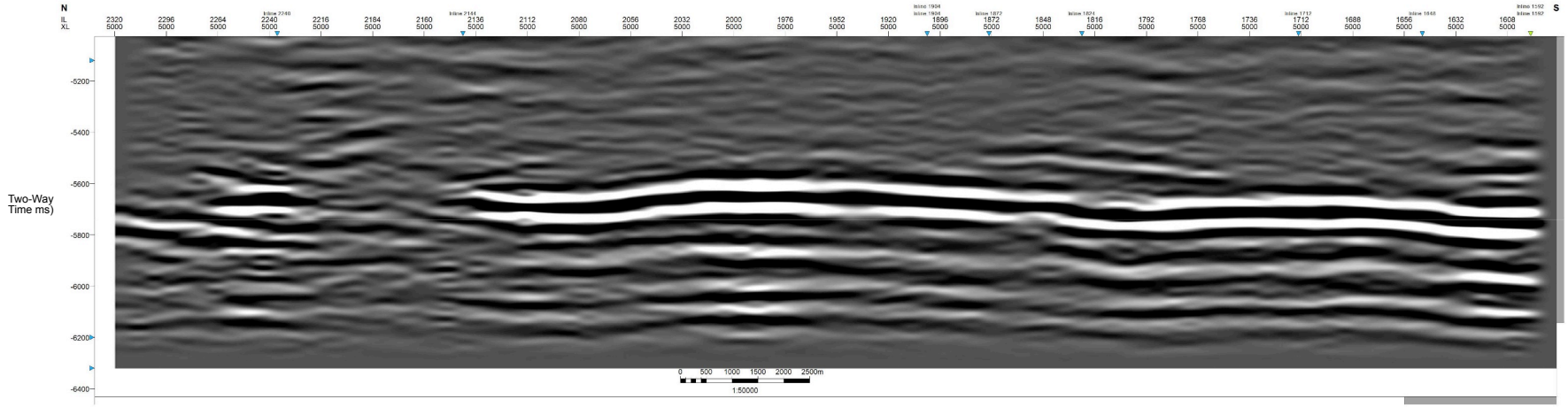

Figure 4.3a Xline 5000, located at the eastern edge of the northern survey area. Two-way time is displayed in ms. Vertical exaggeration of ~1.7 assuming a lower crustal velocity of 6000 m/s.

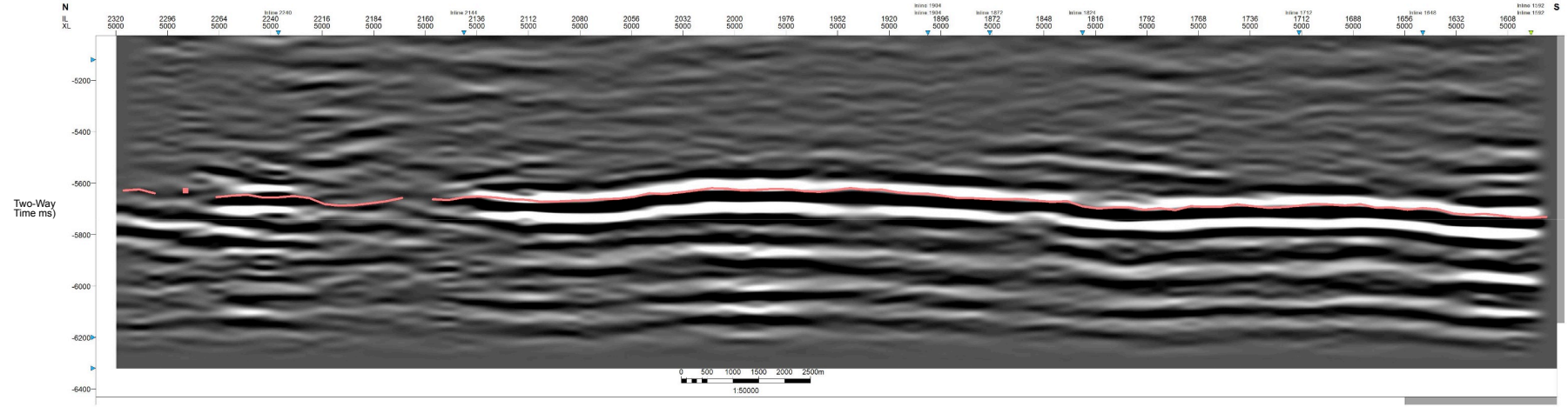

Figure 4.3b Xline 5000, located at the eastern edge of the northern survey area with the composite MOHO horizon displayed. Two-way time is displayed in ms. Vertical exaggeration of ~1.7 assuming a lower crustal velocity of 6000 m/s. Composite MOHO horizon picks displayed in red

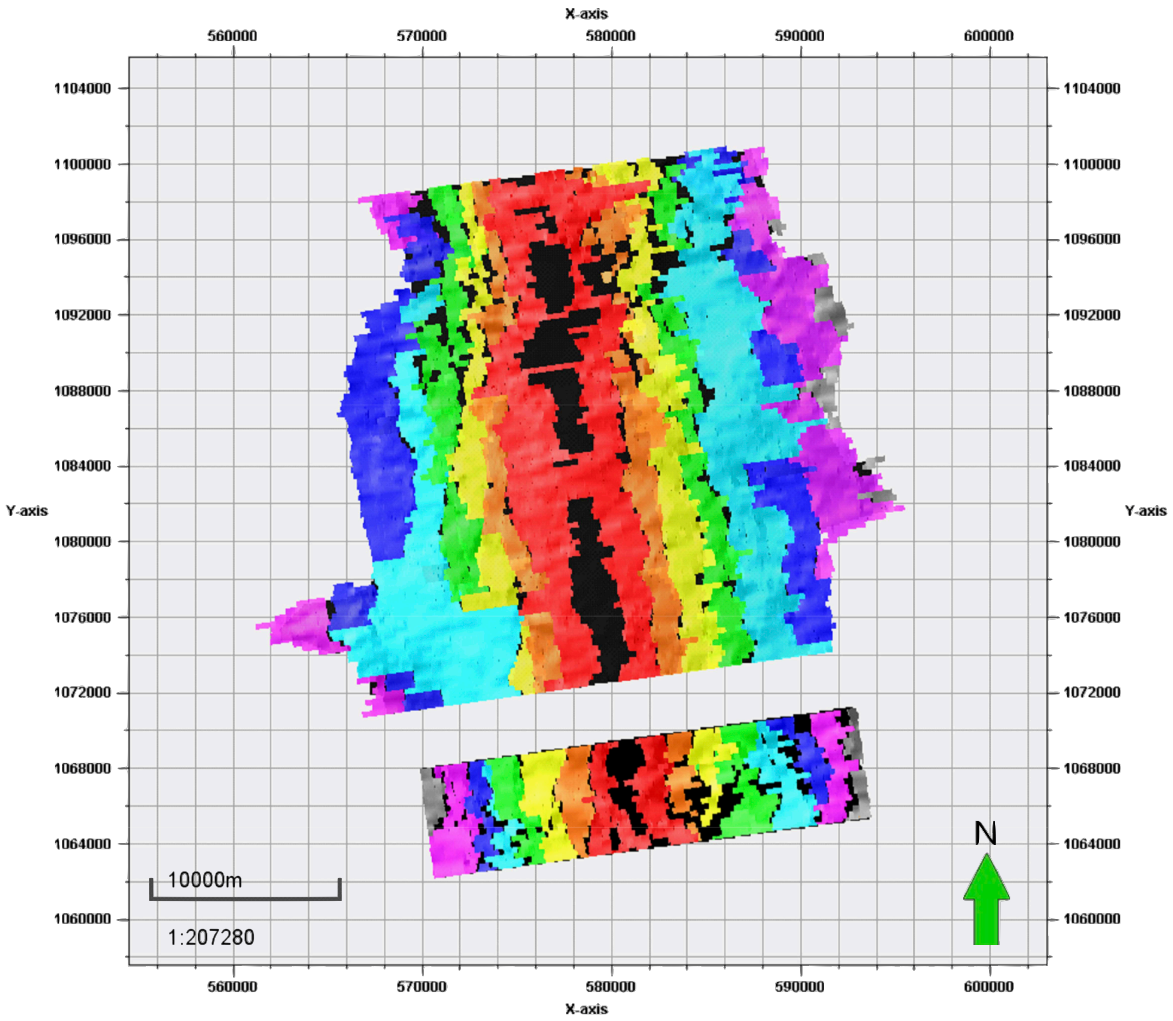

Figure 4.4 Main MOHO reflection horizons group into individual terraces, which are distinguished by different colors: terrace 1 red, 2 orange, 3 yellow, 4 green, 5 cyan, 6 blue, 7 pink, and 8 grey. Both axes are distance in meters with original latitudes and longitudes converted to UTM using geodetic reference frame WGS84 and zone 13N.

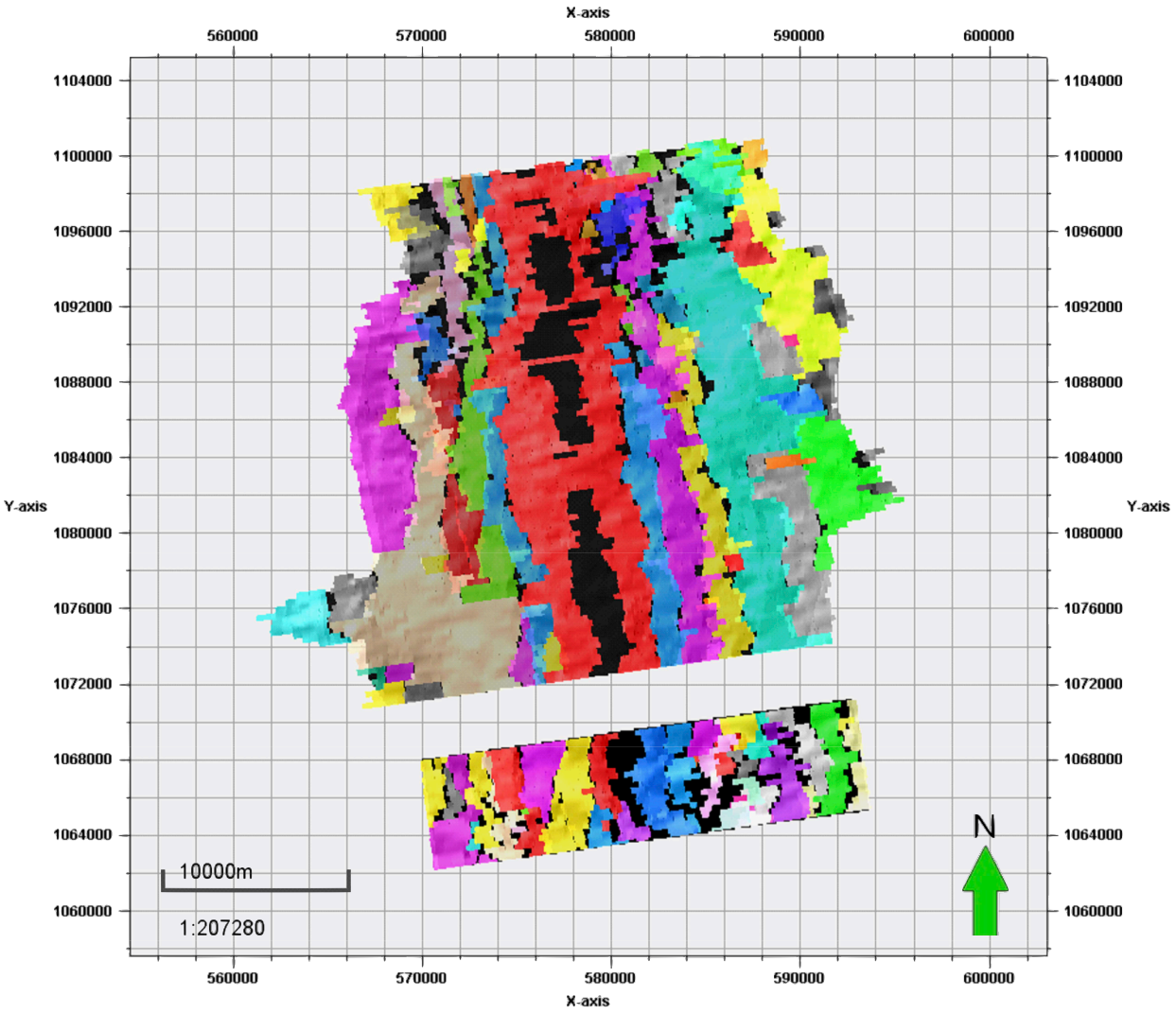

Figure 4.5 Raw main MOHO reflection horizons displayed as individual horizons, which are distinguished by different colors that were arbitrarily defined. Both axes are distance in meters with original latitudes and longitudes converted to UTM using geodetic reference frame WGS84 and zone 13N.

4.2 Impulsive MOHO

Impulsive MOHO is observed along the flanks of the ridge but is significantly more pronounced in the SW corner and east-central section in the northern survey area (Figure 4.6 & 4.7). In Figure 4.6, a high amplitude reflection of the MOHO stretches over 8 km from the western edge of the survey area to within 5 km of the ridge axis. Along the eastern flank of the ridge the outermost reflections periodically merge forming a large impulsive reflection that extents over 5 km, from the edge of the survey area to within 9 km of the ridge axis. The impulsive horizons consist of high amplitude reflections overlain by OLRs. In both areas, the impulsive Moho arrival

time is ~60 ms earlier than the surrounding MOHO, thus forming anticlinal structures parallel to the ridge axis (Figures 4.6, 4.7 & 4.8).

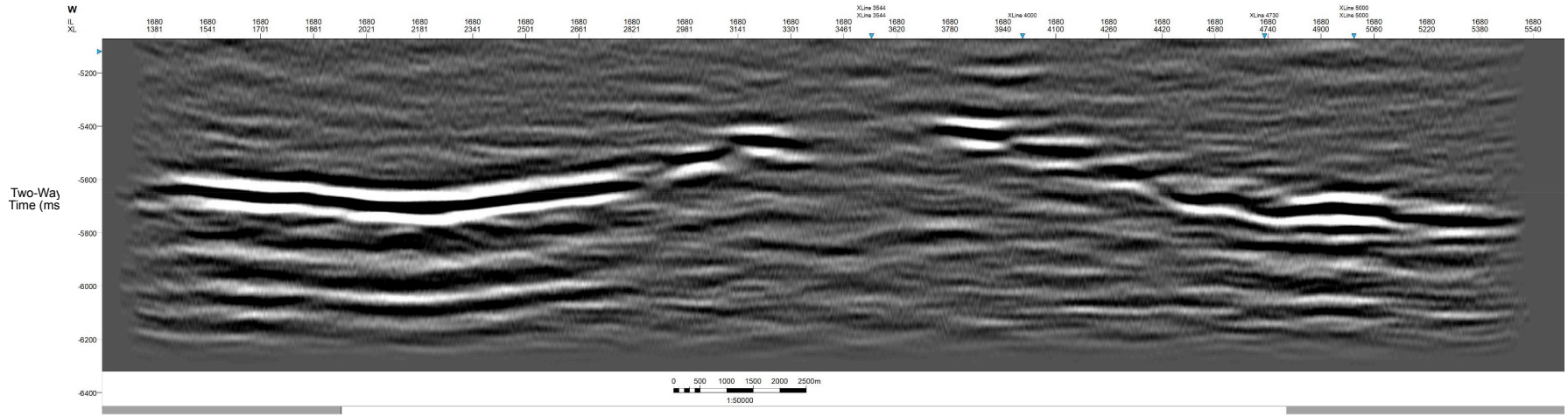

Figure 4.6a Inline 1680, located in the southwestern corner of the northern survey area. Two-way time is displayed in ms. The impulsive MOHO on the western ridge flank arrives at shorter TWT than on the eastern side. Vertical exaggeration of ~1.6 assuming a lower crustal velocity of 6000 m/s.

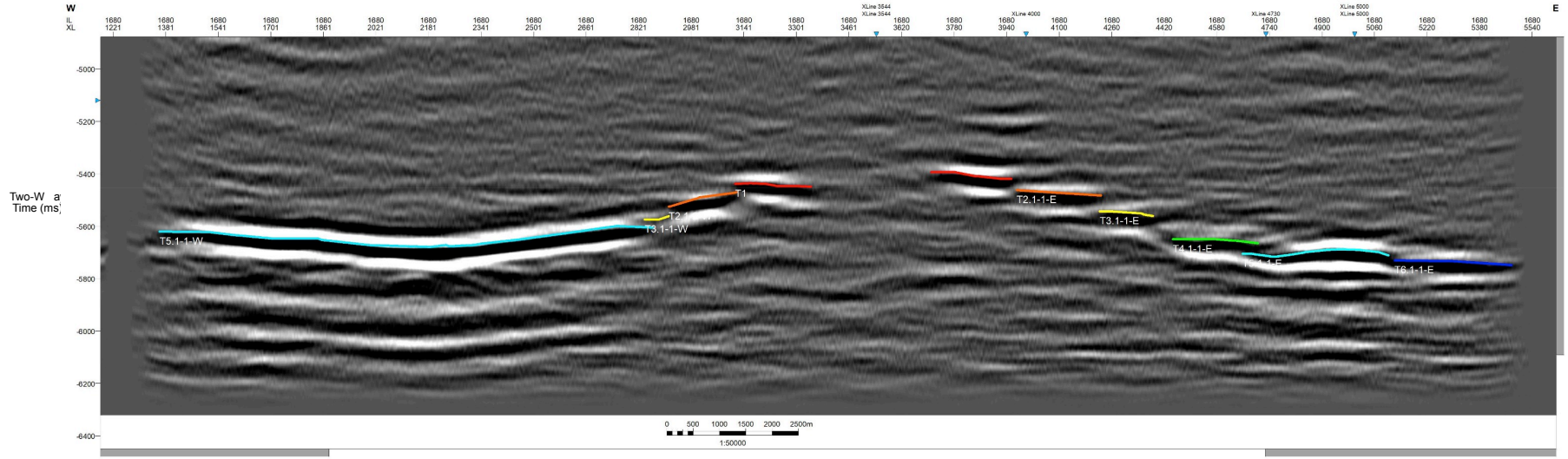

Figure 4.6b Inline 1680, located in the southwestern corner of the northern survey area. Two-way time is displayed in ms. Vertical exaggeration of ~1.6 assuming a lower crustal velocity of 6000 m/s. The picked MOHO reflections are displayed using different colors to distinguish between terraces: 1 red, 2 orange, 3 yellow, 4 green, 5 cyan, 6 blue, and 7 pink.

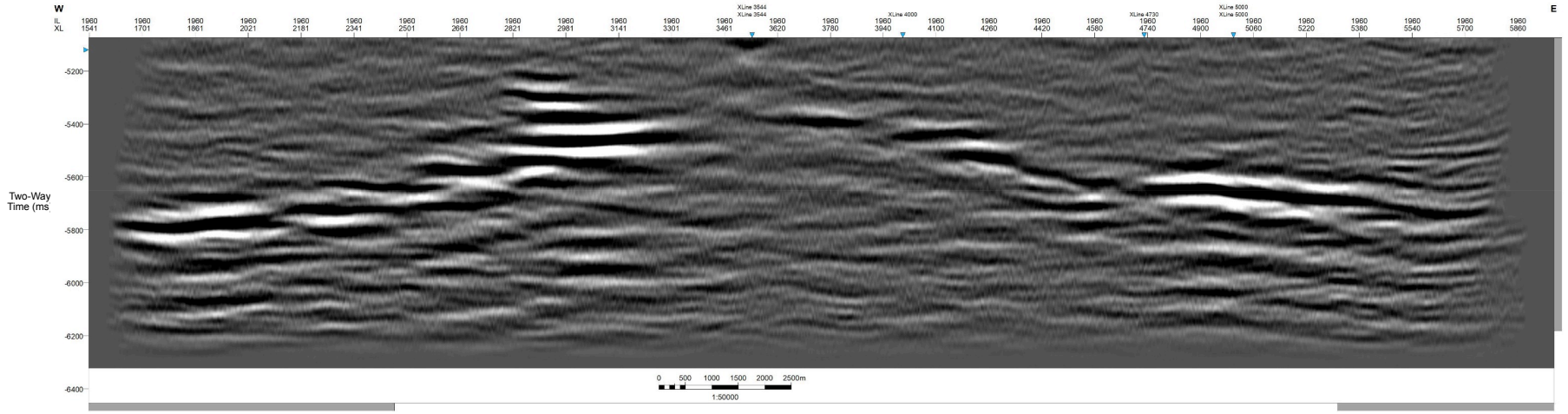

Figure 4.7a Inline 1960, located in the middle of the northern survey area. The impulsive MOHO on the eastern ridge flank is significantly larger in total area than the impulsive MOHO at the edge of the western flank. Two-way time is displayed in ms. Vertical exaggeration of ~1.7 assuming a lower crustal velocity of 6000 m/s.

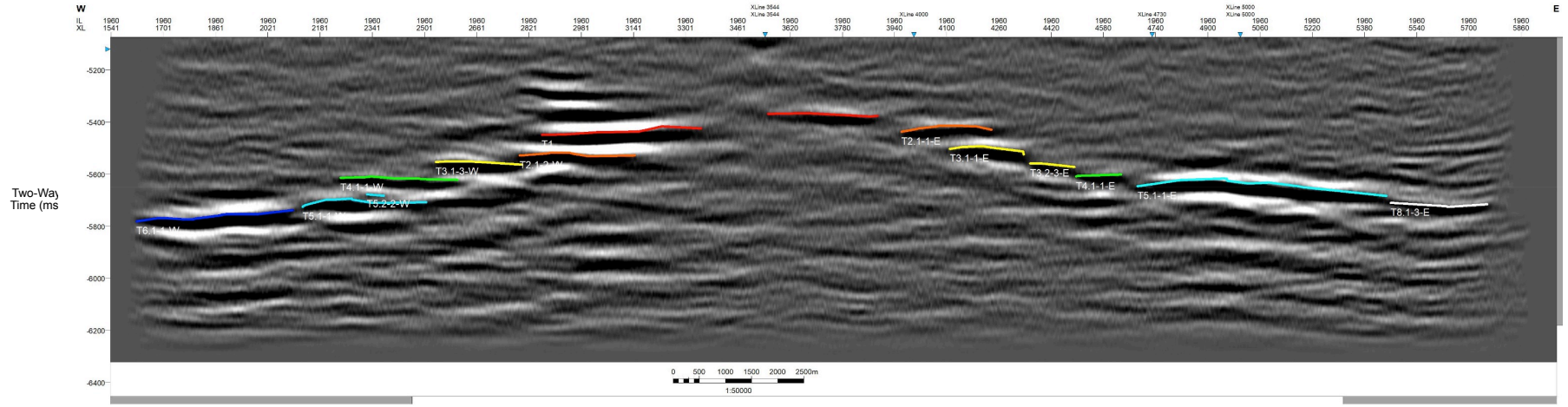

Figure 4.7b Inline 1960, located in the middle of the northern survey area. Two-way time is displayed in ms. Vertical exaggeration of ~1.7 assuming a lower crustal velocity of 6000 m/s. The main MOHO picked reflections are displayed using different colors to distinguish between terraces: 1 red, 2 orange, 3 yellow, 4 green, 5 cyan, 6 blue, and 7 pink.

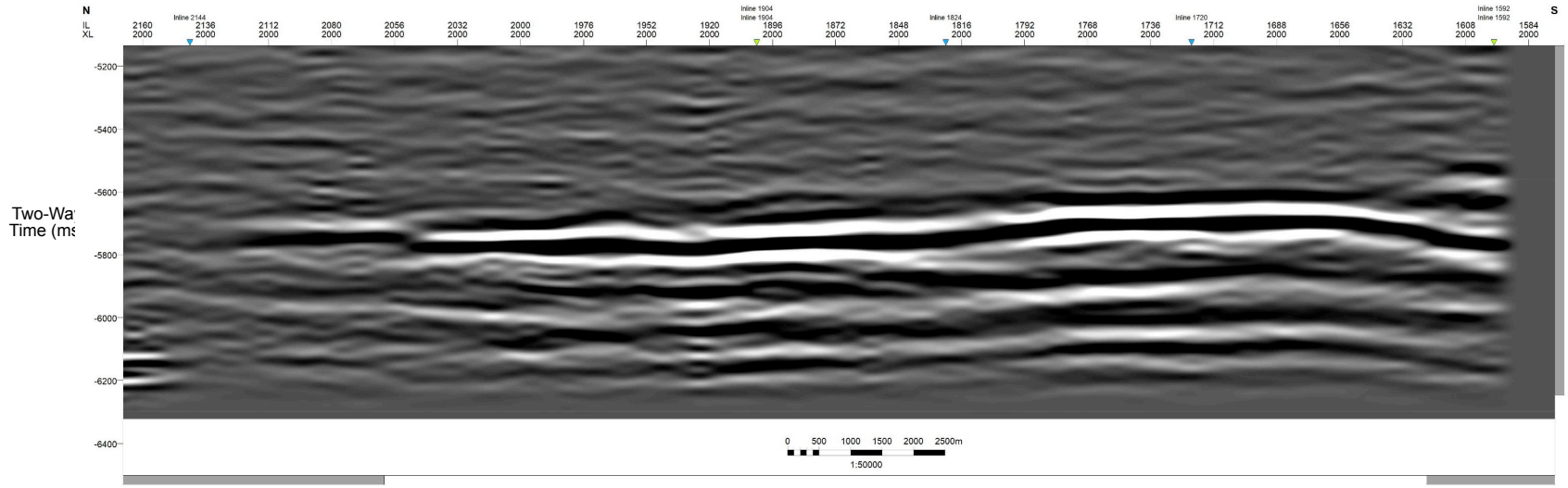

Figure 4.8a Xline 2000, located along the western edge of the northern survey area. TWT is displayed in ms. Vertical exaggeration of ~1.7 assuming a lower crustal velocity of 6000 m/s.

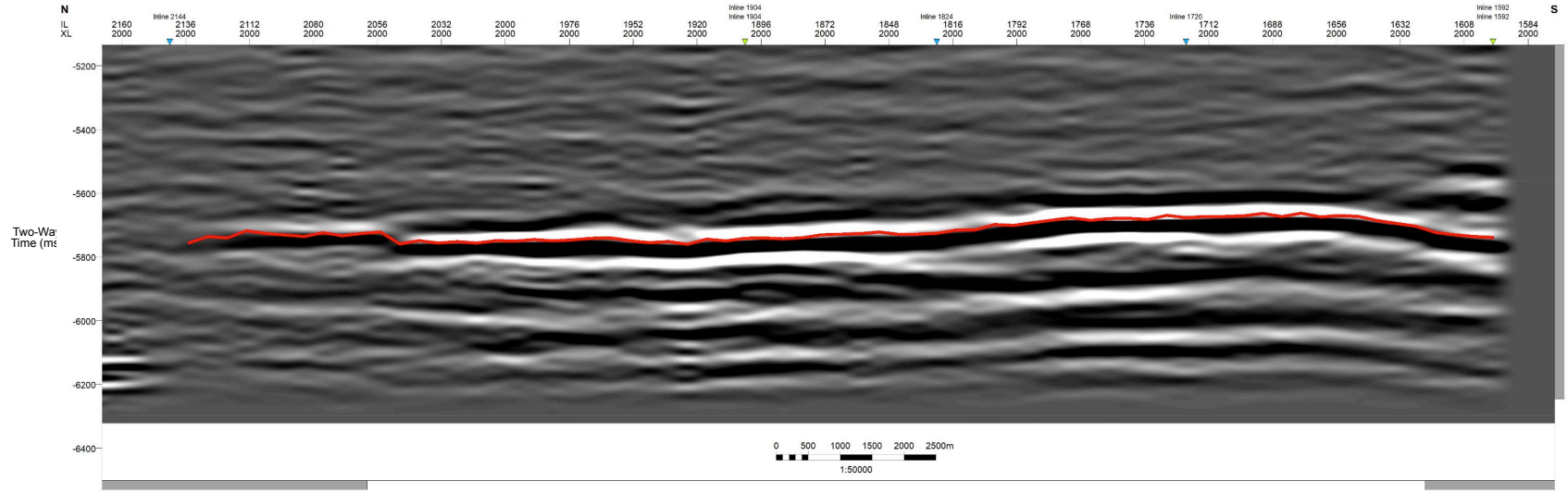

Figure 4.8b Xline 2000, located along the western edge of the northern survey area. TWT is displayed in ms. Vertical exaggeration of ~1.7 assuming a lower crustal velocity of 6000 m/s. The picked composite MOHO horizon is displayed in red.

4.3 Composite MOHO Horizon

The interpretation of the composite MOHO horizon provides a good insight into the geometry and structure of the MOHO Discontinuity. The MOHO is mostly symmetrical at the MOR with terraces located at similar TWT on either side of the ridge. As can be seen in Figure 4.9, along the MOR the MOHO is composed of very closely spaced terraces that trend parallel to the ridge axis. These terraces are continuous along most of the investigated ridge, but are less clear in the northern third of the northern survey area and for the majority of the southern survey area. Along the edges of the survey area, the shallower dipping (in TWT) MOHO converges northwards towards the ridge axis. In the composite horizon the impulsive MOHO reflections are at later TWTs. In the SW corner of the survey area, impulsive MOHO is significantly larger than elsewhere in the survey area, extending up to the 2nd terrace, covering an area that is ~8 km long in the ridge-parallel direction. In comparison, on the eastern ridge flank, impulsive MOHO extends >15 km parallel to the ridge but only extents up to the 4th terrace (Figures 4.4 & 4.9). Along each of the ridge flanks there are multiple impulsive MOHO reflections but these are typically limited to the outer edge of the survey area (Figure 4.5).

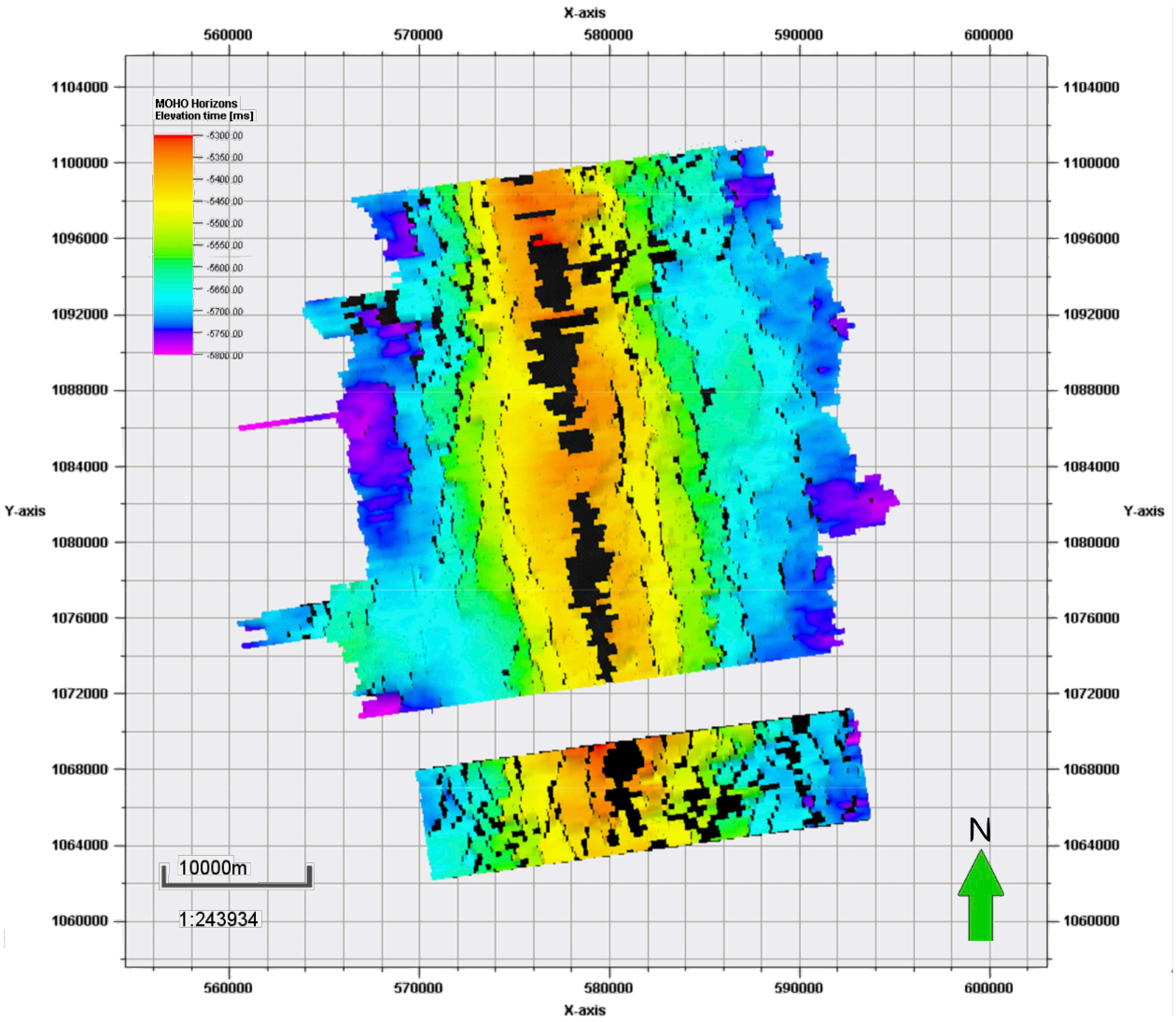

Figure 4.9 MOHO reflection surface displayed in ms TWT (colour scale). Both axes are distance in meters with original latitudes and longitudes converted to UTM using geodetic reference frame WGS84 and zone 13N. Black background used to increase contrast where no MOHO reflection was picked.

4.4 Off Lapping Reflections (OLRs)

Extensive linear low amplitude reflections are observed above the MOHO reflections (Figures 4.10 & 4.11). These reflections appear to off lap from the lip of each MOHO terrace and many of these reflections (OLRs) not only float out over lower terraces but also extend parallel to the ridge for the length of the survey area (Figures 4.12, 4.13 & Appendix). The dip of the reflections varies greatly and can dip either toward or away from the ridge but most are near horizontal. Along the fringes of the ridge the OLRs typically conform to the shape of the MOHO. The OLRs vary in length from <1 km to > 30 km parallel to the ridge but have a width of ~1 km up to a

maximum length of ~9 km in the survey area. Some terraces appear to have multiple OLRs associated with them. The shallowest OLR (OLR0) doesn't conform to any terrace, as it is located directly above the ridge axis. The largest OLRs (0 through 4) were observed across the majority of the survey area all (except OLR 0) conform to the shape of the terraces where they abut the ridge. In contrast OLRs5 through OLRs7 are much more discontinuous. Smaller OLRs are observed throughout the survey area and typically are only present along a few inlines. The OLRs above impulsive MOHO span the length of the MOHO reflections. Above the impulsive MOHO at the SW corner of the northern survey area, OLR4 splits into multiple smaller horizons that dip both towards and away from the ridge axis (Figure 4.11b).

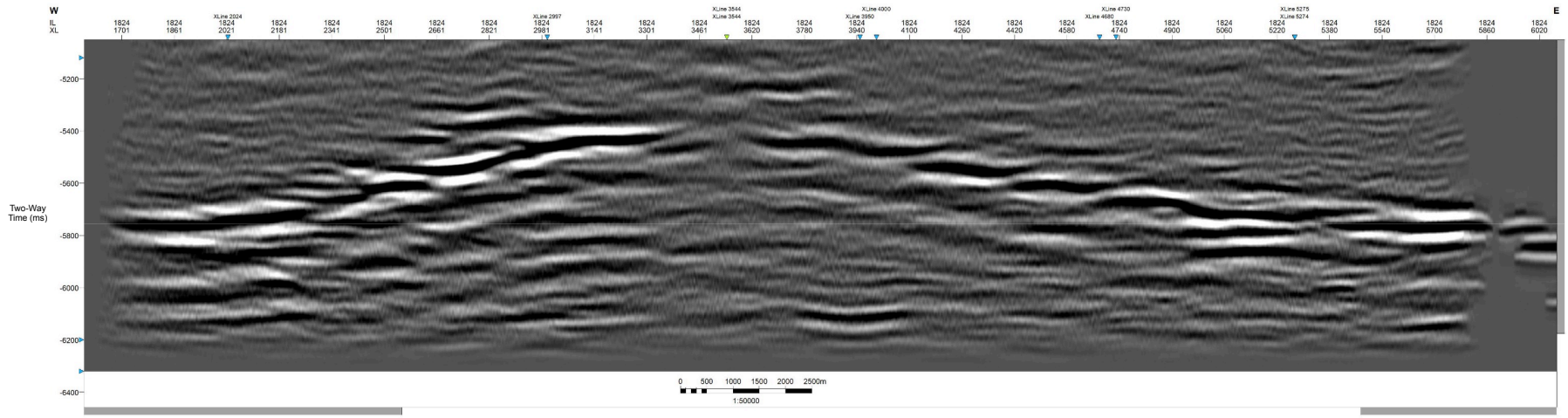

Figure 4.10a Inline 1824 located on the mid-southern section of the northern survey area. Two-way time displayed in ms. Vertical exaggeration of ~1.7 assuming a lower crustal velocity of 6000 m/s.

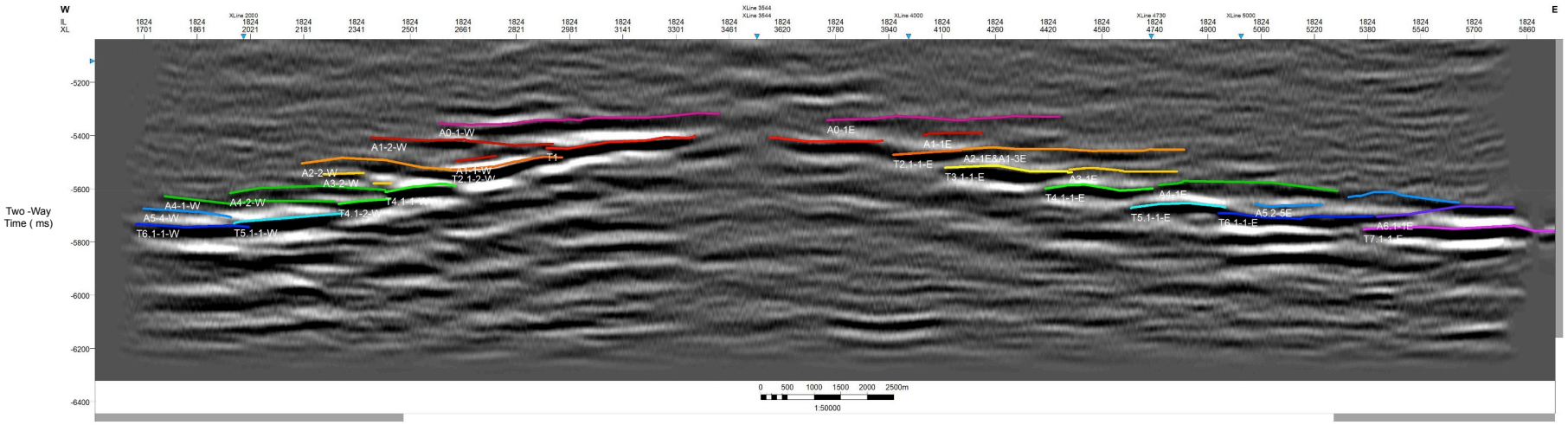

Figure 4.10b Inline 1824. Two-way time displayed in ms. Vertical exaggeration of ~1.7 assuming a lower crustal velocity of 6000 m/s. The main MOHO reflections and off lapping reflections are displayed using colors to distinguish between different reflection MOHO terraces and associated off lapping reflections: 0 maroon (no observed terrace), 1 red, 2 orange, 3 yellow, 4 green, 5 cyan, 6 blue, and 7 pink.

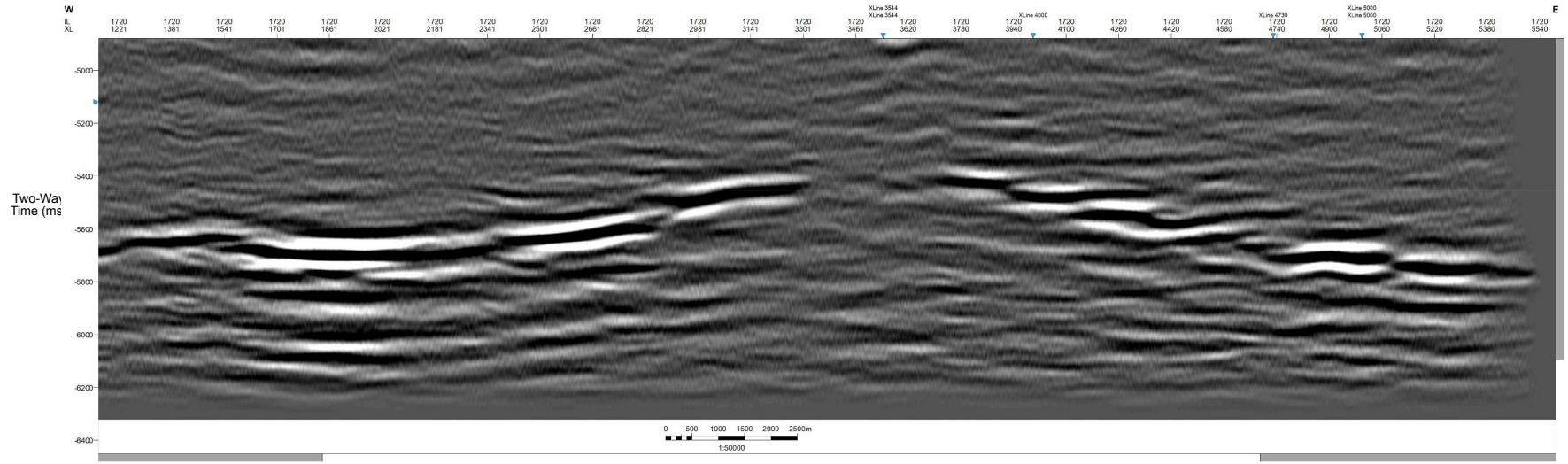

Figure 4.11a Inline 1720. Two-way time displayed in ms. Vertical exaggeration of ~1.6 assuming a lower crustal velocity of 6000 m/s.

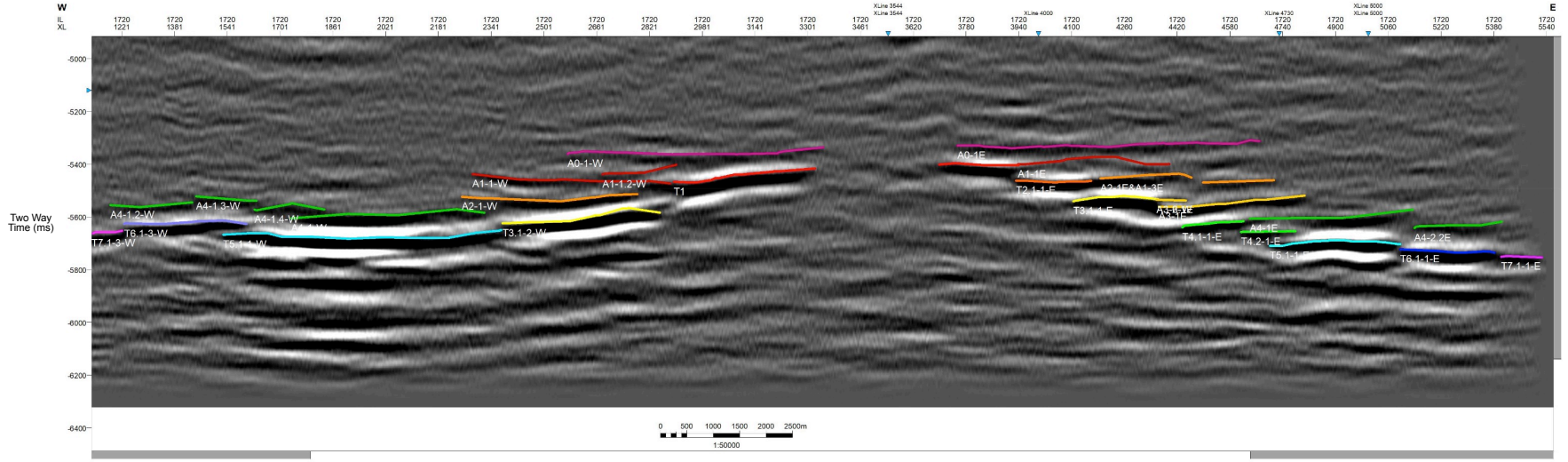

Figure 4.11b Inline 1720. Two-way time displayed in ms. Vertical exaggeration of ~1.6 assuming a lower crustal velocity of 6000 m/s. The MOHO reflections and off lapping reflections are displayed using different colors to distinguish between different reflection MOHO terraces and associated off lapping reflections: 0 maroon (no observed terrace), 1 red, 2 orange, 3 yellow, 4 green, 5 cyan, 6 blue, and 7 pink.

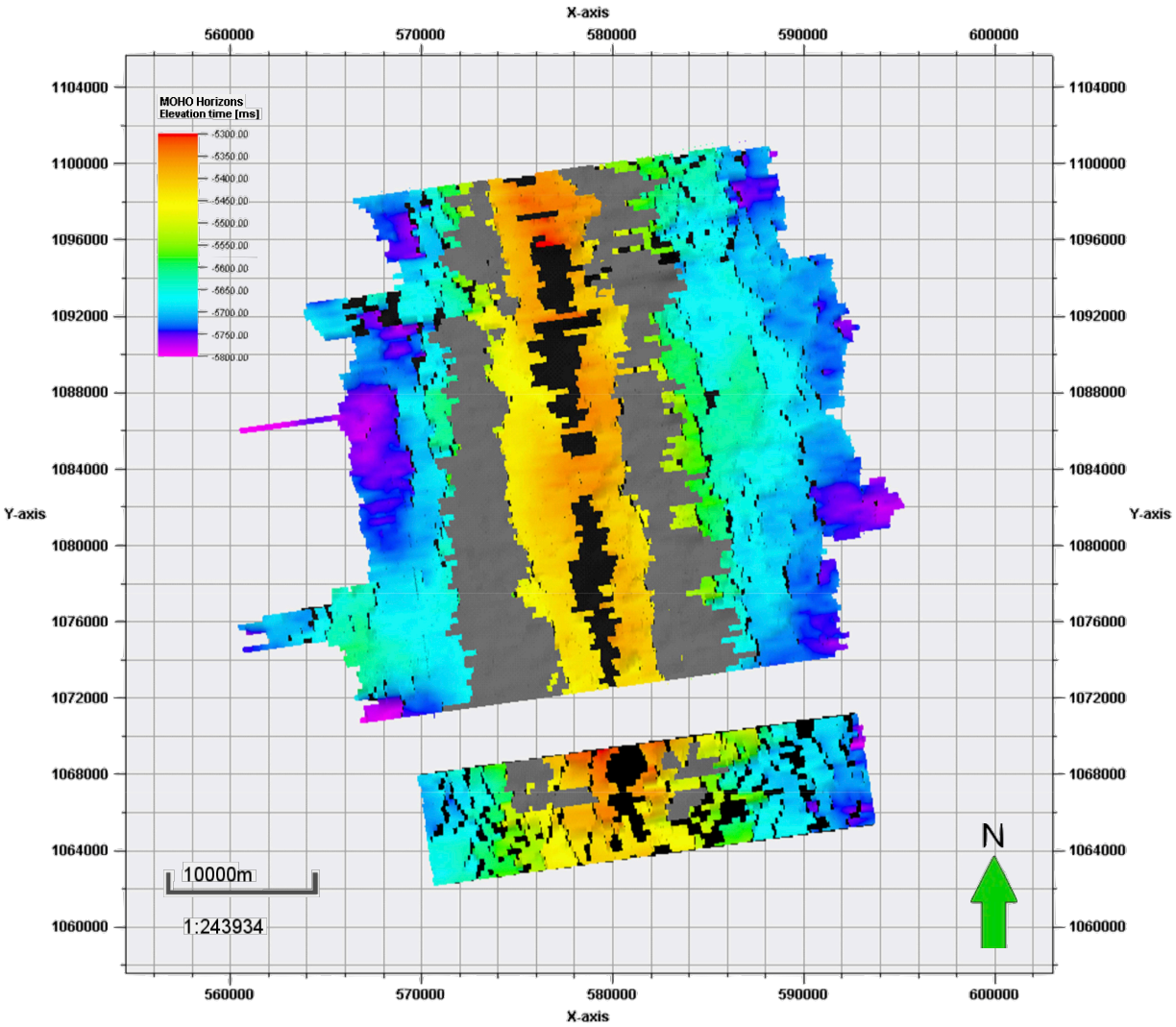

Figure 4.12 OLR 1 (grey) off lapping from the top terrace (T1) on either side of the ridge, displayed on top of the reflection MOHO horizon (Figure 4.9). Colour scale indicates TWT; black background added to increase contrast for areas where reflection MOHO was not possible to pick. Both axes are distance in meters with original latitudes and longitudes converted to UTM using geodetic reference frame WGS84 and zone 13N.

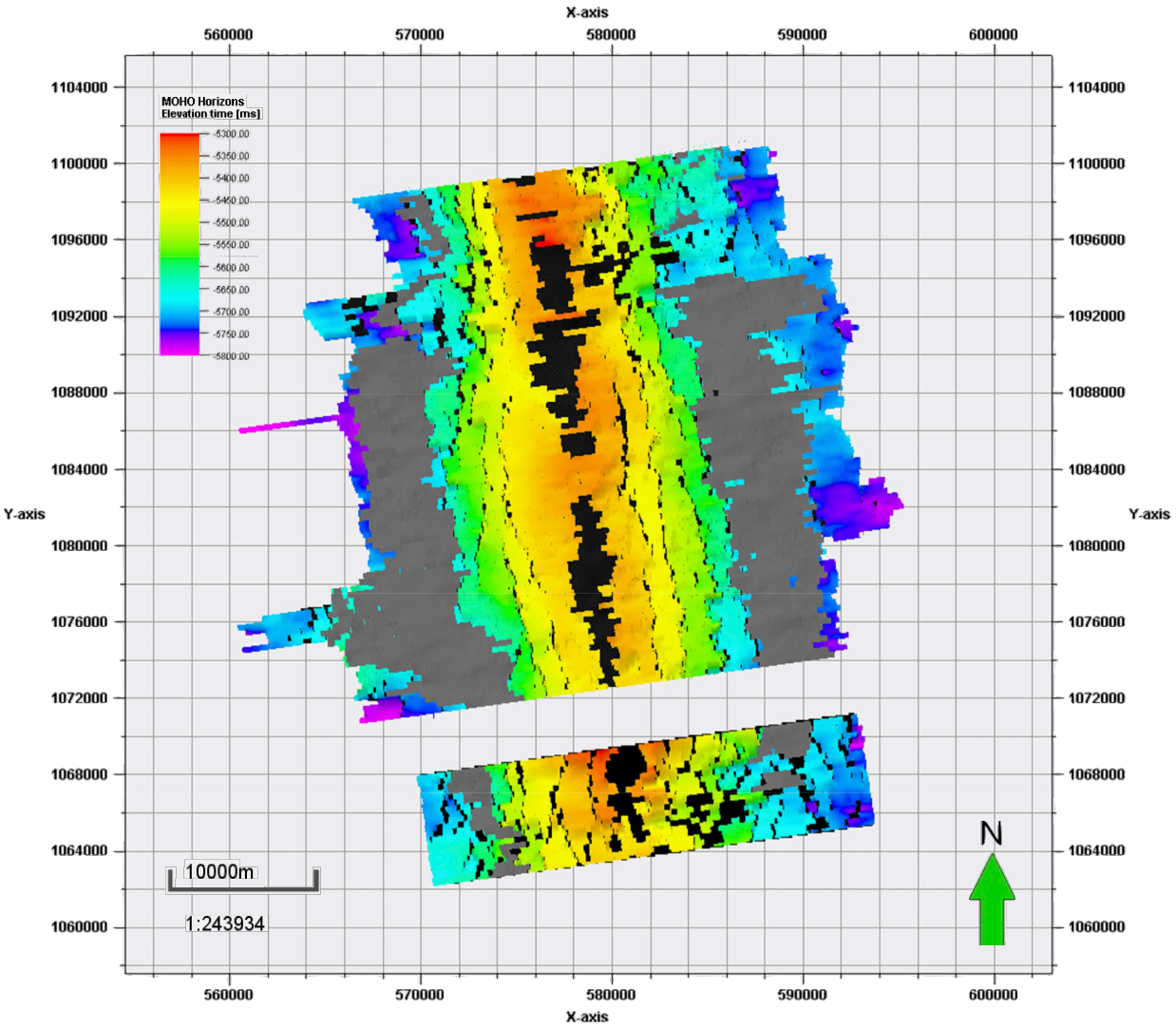

Figure 4.13 OLR 4 (grey) off lapping from terrace T4 on either side of the ridge, displayed on top of the reflection MOHO horizon (Figure 4.9). Colour scale indicates TWT; black background added to increase contrast for areas where reflection MOHO was not possible to pick. Both axes are distance in meters with original latitudes and longitudes converted to UTM using geodetic reference frame WGS84 and zone 13N

5.0 DISCUSSION

The interpretation of MOHO and nearby reflection events from the EPR 3D prestack migrated reflection volume has resulted in identification and detailed description of multiple structures that had not been previously observed or had only been described in 2D from sparse regional MCS profiling work [*Barth and Mutter, 1996* ; *Kent et al., 1994*; *Nedimović et al., 2005*]. These include the shingling of the reflection MOHO that has been interpreted here as due to terraces,

and off lapping structures that stem from these terraces and have been interpreted here as large sills intruded in the lowermost oceanic crust. The properties and potential causes of these structures are discussed in this section.

5.1 MOHO Terracing

Throughout the survey area the MOHO is observed to be composed of 6-7 terraces along the flanks of the EPR (Figure 4.9). Each of these terraces is vertically offset from the next underlying terrace by about ~170 m, assuming an average oceanic crustal velocity of 6000 m/s, and the terraces typically display minor overlap that maybe a relic from the migration of the data [*Aghaei, 2013*]. The spacing of the terraces is similar to the horst and graben topography observed at the seafloor [*MacDonald et al., 1996*], with multiple steps that are vertically offset by normal faulting. This suggests that the terracing of the MOHO is the result of normal faulting, which is not surprising because mid-ocean ridges are extensional systems. At the ridge crest the first terrace terminates approximately 2.0 km from the ridge axis along the eastern and western flanks. This distance matches with numerical models that have shown that hydrothermal circulation significantly reduces the temperature of the crust beginning about 2 km from the ridge [*Dunn et al., 2000*; *MacLennan et al., 2004*]. Cooling at MOHO depths would greatly reduce the plasticity of the nearby crust at greater distances.

The offset between terraces isn't always a sharp contact since the terraces frequently merge and split parallel to the ridge axis throughout the survey area. This is likely caused by discontinuous faulting and differential subsidence of the MOHO during faulting. This can be seen, for example in the merger of terraces 2 and 3 in the southwestern half of the northern survey area (Figure 4.9).

Each terrace is composed, along axis, of 1-3 MOHO reflections with a few smaller MOHO reflections that display no or little overlap. The presence of multiple MOHO reflections per terrace is due to the merging and splitting of the terraces along the ridge. The majority of the MOHO reflections are highly continuous, especially near the ridge axis; however the merging of

terraces further away from the ridge results in the absorption of the smaller MOHO reflections into the larger ones. In the northern half of the northern survey area and in the southern survey area, reduced resolution due to magmatism and increased structural complexity in the crust results in greatly diminished amplitude of the reflection MOHO and, therefore, less certainty and continuity of the picking. In this area, the termination of the MOHO reflections and the decreased abundance of smaller MOHO reflections is caused by the decreased resolution and is not an accurate representation of the terraces. It is expected that terraces in the areas of decreased resolution are continuous across the survey area, similar to what is observed in the southern half of the northern survey area.

5.2 Off Lapping Reflections (OLRs)

The OLRs are observed as planar low amplitude reflections that off lap from the outward edges of the terraces. Because the low amplitude OLRs originate at the high amplitude MOHO terraces, it is not always possible to image their reflections at the MOHO. Typically the OLRs are observed as a single reflection extending as much as 8 km from the edge of the terrace; however in some instances part of the reflection was masked causing the OLR to appear as multiple smaller reflections. In Oman, Nicolas et al. [*2015*] identified multiple dunite, wehrlite and olivine gabbroic sills in ophiolites that had been injected into the lower crust just above the MOHO. These sills could correspond to the off lapping reflections observed at the MOHO. As observed in Figures 4.11 & 4.12, the thin ORLs extend over a large area and could represent periodic injections of magma into the lower crust as sills. The exact dip of the sills is uncertain as they were interpreted in TWT and not in depth; however the sills typically trend close to the horizontal (constant TWT) suggesting little to no dip.

The injection of magma into the crust in the form of sills is due to either an increase in magmatic head pressure or a drop in lithostatic pressure. In either case, as magma rises from the mantle, the head pressure exerted by the magma may be enough to overcome the lithostatic pressure and inject magma into the lower crust. This results in gabbroic and

ultramafic magma from the mantle forming very broad and thin magma bodies intruding into the massive gabbro of the lower crust, possibly causing the entire crust to be uplifted. The point of injection of the sill into the crust must be located close to the axis of the ridge because OLR0, the shallowest and youngest OLR, has been identified within 1 km of the ridge axis.

In order for melt to be injected into the crust, a significant amount of magma would have to accumulate in the upper mantle, increasing the pressure it exerts on the crust before it is released. At the EPR, melt builds up below the MOHO where it is fed to the AML via feeder dykes or percolation. Because this process causes deformation of the crust, the process is dependent on the rigidity of the lower crust and upper mantle and the pressure that is exerted upon it. If the input of magma to the AML were reduced or blocked, magma would build up at the base of the crust, increasing the pressure that it exerts on the lower crust. Once the magma at the base of the crust reached a high enough pressure, a drop in lithostatic pressure could result in the magma at the base of the crust being over pressured, causing magma to be injected into the crust. It is unclear what mechanism could increase the lithostatic pressure at the EPR. One possible cause might be periodic sea level changes associated with glaciation which could produce a change of pressure of ~10^4g/cm^3 (see below). It may also be possible that lithological barriers such as earlier dunite sills, can prevent magma from migrating up into the crust, causing magma to accumulate at the MOHO [*Nicolas et al., 2015*]. Gradually the pressure would increase as more magma accumulates until the pressure causes the barrier to fracture, injecting the magma into the lower crust.

5.3 Structural Constraints

Currently it is not possible to fully and confidently explain all of the processes involved in the formation of the terraced MOHO and OLRs observed at the EPA. However any process that explains these features must take into account the following observations or constraints:

1. Physical configuration of the terraces and sills. The MOHO is composed of multiple terraces (6 on the western flank and 7 on the eastern flank of the ridge, with maximum crustal ages of ~216 Ka and ~260 Ka, respectively, assuming a half spreading rate of 5.5

cm/yr) with nearly horizontal sills off lapping from the edges of the terraces. The MOHO forms a single terrace at the ridge crest and is less impulsive with multiple closely spaced terraces on either side. Further from the ridge the terraces are more impulsive and spread out. Both the terraces and sills are episodic.

2. Sills abut terraces, but are not cut by faults from deeper terraces.

3. Fault plane solutions for ridge earthquakes between transform faults in the upper crust area consistent with normal faulting. The lower crust is aseismic suggesting that if faults are active below layer 2, the deformation is plastic, thus aseismic [*Sykes, 1967*].

4. The correlation between the half width of the top of the MOHO ridge (T0) before the first terrace, the ridge axis itself at the seafloor, the AML and the width of the axial high temperature zone to the "cold wall" in axial thermal models, all ~2 km wide.

5. Active faulting on the small horsts and grabens on the seafloor dies away from the ridge with outward-facing growth faults becoming inactive by ~6 km away from the ridge axis and the ridge-facing normal faults ceasing to grow by ~30 km [*MacDonald et al., 1996*].

6. The MOHO becomes impulsive off the ridge axis. At the ridge flanks the terraces begin to merge, forming the larger segments of impulsive MOHO observed in non-MOR environments.

7. Continuous accretion of oceanic crust by seafloor spreading. The accretion of new crust and upper mantle is continuous at a half rate of 55 mm/yr in the survey area [*Carbotte and Macdonald, 1992*].

8. Mantle Drag. Faster motion of the mantle away from the ridge relative to the crust causes shear deformation in the lower crust and upper mantle. In the ophiolites this is

seen as intense shear deformation in the lower crust parallel to the MOHO [*Nicolas et al., 2015*].

5.4 Evolution of the MOHO and Sills

It is clear from the images and discussion presented above that the MOHO at the ridge crest of the EPR is cut by terraces and that the lower crust immediately overlying the MOHO is periodically injected by sills. The impedance contrasts required for imaging in this environment suggest that the sills consist of dunite or wehrlite intruding gabbro, as seen in the MOHO transition zone in ophiolites such as Oman or the Bay of Islands [*Nicolas, 1989*; *Collins et al., 1986*].

Numerous magmatic and tectonic models can be proposed to explain these features, but few are consistent with all of the constraints listed above. Older models involving large magma chambers (eg. *Pallister and Hopson, 1981*) appear to be precluded by the absence of steady-state magma chambers at the base of the crust in marine seismic data, including the cube investigated here. Similarly, tectonic models involving mantle drag-induced thrust faulting of the MOHO at the ridge appear to be inconsistent with the off-ridge reversal in shingling sense observed in the southwest corner of the northern survey area, since reversals in the mantle flow direction would seem impossible on such small scales (constraint 8).

Nonetheless, the configuration of the terraces in cross-section and map plan (Figure 4.9) suggests that they are structurally controlled. One model that is at least consistent with the constraints listed above is that the MOHO terraces are formed by normal faults (constraint 3) connected to the horsts and grabens (constraint 5) at the seafloor. To meet the constraint that the fault is seismic in the shallow crust but aseismic in the lower crust and upper mantle, the fault would have to be located in the 1000-1100°C isotherm in the near-vertical, high T-gradient wall (constraint 4) observed in thermal models of the ridge and attributed to hydrothermal cooling [*Dunn et al., 2000*; *MacLennan et al., 2004*]. This would be consistent with some of the near-vertical, crust cutting faults observed in Oman, which are aligned parallel to the sheeted dikes (ie, the ridge), widen with depth and display brittle deformation in the upper crust and

plastic shear deformation in the lower crust, where they sole in the MOHO [*Nicolas, 1989*]. This model requires a re-purposing of some of the faults observed in Oman, since Nicolas (*1989, 2015*) attributed most of them to obduction-related deformation.

To conform to structural constraints 1, 2, and 7, it is proposed that all of the sills are generated at the top of the axial MOHO high. As the crust moves away from the ridge by sea floor spreading through the "thermal wall" modelled by MacLennan et al (*2014*), it loses the vertical support provided by mantle and magmatic upwelling, it cools and contracts and a normal fault develops, creating the first terrace at the 1000-1100°C isotherm. Since the sill, originally overlying the MOHO on the top of the ridge crest, also moved off-axis, it is cut by the fault and rides down with the terrace. If the sill is replenished at the ridge crest and re-extends out over the fault, the stage is set for a repeat of the terracing event as the seafloor continues to spread. In this way, only two normal faults are involved in the creation of the terraces (one on either side of the ridge axis), each sill abuts its defining terrace wall toward the ridge, yet floats out over deeper terraces (Figures 4.12, 4.13 & Appendices) without being cut again by faulting. It should be noted that a variant of this model, in which the sills are fed by magma coming up the fault instead of the center of the MOHO high, appears to meet most of the constraints as well, but doesn't generate sill A0.

Several questions remain. Why do the terraces begin to merge together as they move away from the ridge axis, forming large bodies of impulsive MOHO at the edge of the survey area? It is difficult to assess this with certainty because the TWTs to MOHO have not been converted to depth using in situ velocities, which can be strongly affected by temperature. It is possible that differential fault motion continues but decreases off-ridge as the crest and mantle cool and thus ceases to cut the overlying sills, allowing the terraces to merge. More likely, mantle drag (constraint 8) finally kicks in, smearing the terraces into a single, impulsive horizon.

Why does the MOHO locally shallow off-ridge, as in the southwest corner and the eastern edge of the northern survey area. Again there are several possibilities. The southwest corner anomaly

could be associated with off-axis magmatism; Aghaei et al (*2014*) imaged a lower crustal melt lens in the immediate vicinity. Alternatively, the MOHO surface may be inherently lumpy in response to slow variations in mantle diapirism and melt delivery.

Why does normal faulting and sill injection appear to be episodic at the ridge even if seafloor spreading is continuous? One fascinating, if controversial, possibility is that seafloor magmatic activity is controlled or at least influenced by Milancović cycles [*Crowley et al., 2015*]. Statistical analysis of seafloor bathymetry in well-constrained, high resolution data sets off Australia show spectral energy peaks in sync with Milancović periods of 23, 41 and 100 thousand years. The authors argue that global changes in sea level of ~100 m due to glaciation and deglaciation will cyclically unload and load the seafloor and the underlying mantle, causing cyclical changes in the decompression melting in the upper mantle that feeds ridge crest volcanism. Although the change in pressure is small, ~10^4 g/cm^2, the periodicity of the terraces and sills in the section of the EPR examined in this study is about 40 thousand years, in striking agreement with the 40 ka Milancović peak. If this is correct, perhaps magmatic activity on the EPR is controlled by the weather.

6.0 CONCLUSIONS

6.1 Conclusion

Interpretation of the reflection MOHO and associated reflection events from the 3D image volume collected along the EPR between 9° 37.5'N and 9° 57'N and processed by Aghaei et al [*2014*] provided insights into the structure of the MOHO in a MOR environment. The 3D image volume consists of the northern, larger survey area and southern, smaller survey area separated by a data gap between 9° 40'N and 9° 42'N. MOHO reflections were identified in ~95% of the survey area. The age of the crust within the survey area varies between zero at the ridge crest and ~260 Ka at the eastern edge of the survey area and ~216 Ka at the western edge of the survey area assuming a half spreading rate of 5.5 cm/yr. Image deterioration in the north half of the northern survey area and in the southern survey area, due to increased magmatism in the crust, limited the extent of the interpretation. Examination of the dataset provided insights into

(1) the terracing of the MOHO, (2) the presence of OLRs (sills) and (3) merging of terraces. A tectonic model (4) is proposed that attempts to explain these observations.

(1) *Terracing of the MOHO*. Detailed observations of the MOHO have identified 6-7 terraces that comprise the MOHO at the EPR. These terraces are vertically offset by ~170 m (~58 ms in TWT) and can be observed starting from ~2 km from the ridge axis. This agrees with hydrothermal circulation models that demonstrate a significant reduction in the temperature of the crust beginning ~2 km from the ridge [*Dunn et al., 2000*]. The cooling of the MOHO reduces its plasticity as it moves away from the ridge, allowing extensional faulting as it undergoes thermal subsidence.

(2) *Presence of sills*. Sills were observed as planar low amplitude reflections that off lap from the outward edges of the terraces. These sills were observed as single reflections overlying the MOHO that extend out over a large area up to 8 km from the ridge axis. In Oman, multiple wehrlite and olivine gabbroic sills have been identified in ophiolites that have been injected into the lower crust [*Nicolas and Boudier, 2015*]. These OLRs appear to represent periodic injection of magma in the lower crust as sills, suggesting a build up of magma at the MOHO due to increased lithostatic or magmatic pressure. The build up of magma increases the pressure exerted on the crust. Later, when the strength of the crust is exceeded, the pressure change causes the crust to fracture and magma is injected into the crust forming sills. The cause of the proposed increase and subsequent reduction of the lithostatic pressure in the crust and upper mantle is uncertain; however, periodic sea level change that may be aligned with Milancović cycles is a possible cause for the pressure fluctuations.

(3) *Merging of terraces.* The terraces are very distinct near the ridge axis; however at ~11 km from the ridge the terraces start to merge with each other forming impulsive segments of MOHO. It is difficult to confirm this with high confidence because the data are interpreted in TWT and not in depth using in situ velocities, which can be strongly affected by temperature. The merging of terraces away from the axis of the EPR could be the result of

mantle drag deforming the MOHO and forming the impulsive reflection MOHO response that is observed away from the ridge.

(4) *Tectonic model*. Numerous magmatic and tectonic models can be proposed to explain the features observed in this study, but few meet all of the constraints listed in section 5.3. The configuration of the terraces suggests that they are structurally controlled and are formed by normal faults that are connected to the horsts and grabens at the seafloor. These faults are located in the 1000-1100°C isotherm in the high T-gradient wall observed in thermal models, allowing the faults to be aseismic (ductile) in the lower crust and at the MOHO but seismic (brittle) in the shallow crust. This is consistent with some of the near-vertical crust cutting faults observed in Oman. These faults are aligned parallel to the sheeted dykes (ie. the ridge), and display brittle deformation in the upper crust and plastic shear deformation in the lower crust [*Nicolas and Boudier, 2015*]. The sills are generated near the ridge crest at the axial MOHO high. As the crust moves away from the ridge it reaches the "thermal wall" [*MacLennan et al., 2004*] and begin to cool and contract. This results in normal faulting forming a terrace. Since a sill immediately overlies the MOHO it also moves down with the terrace. If a new sill is formed at the ridge, the cycle is repeated. This results in sills that abut their associated terraces and extends over the deeper terraces.

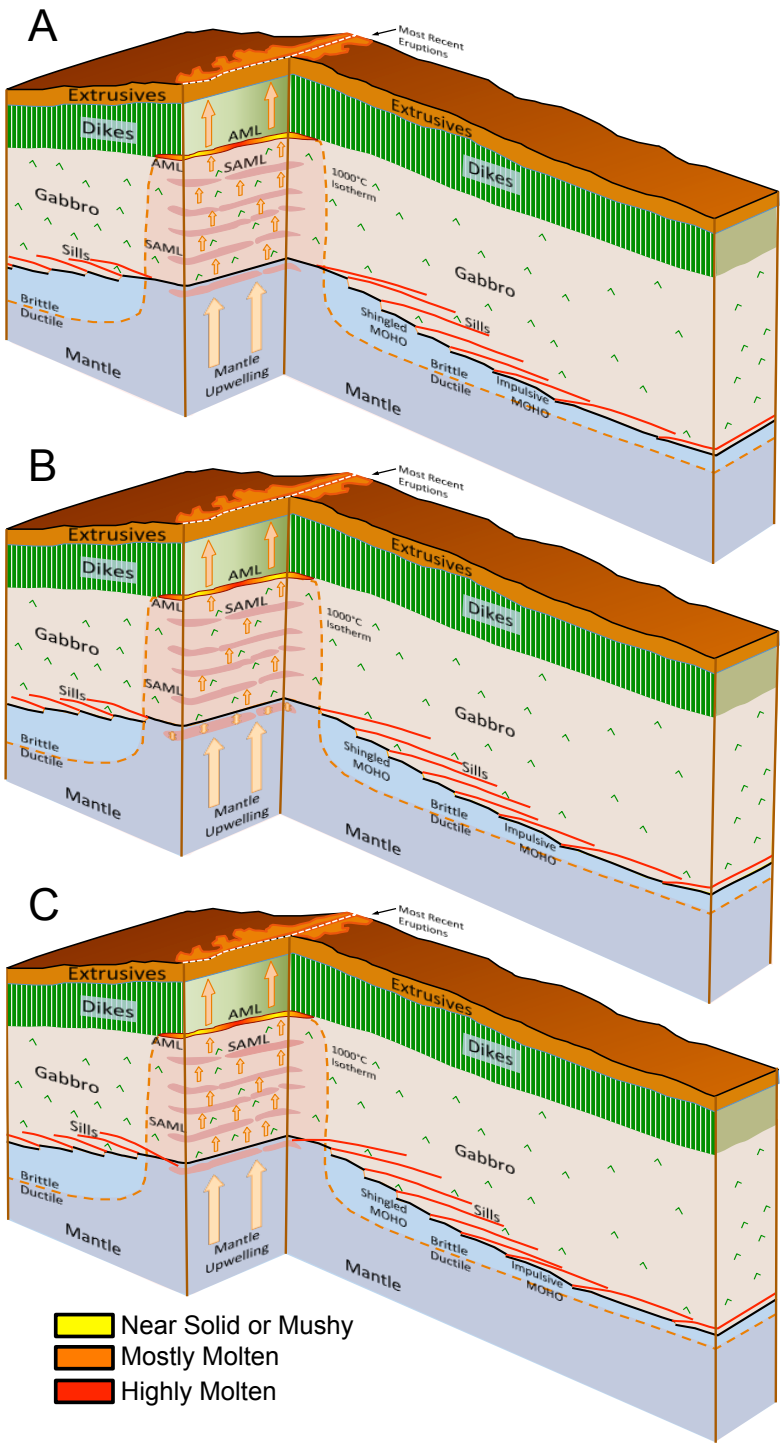

Figure 5.1. Schematic diagram showing the stages involved in the formation of the sills (OLRs) and terraces. Legend describes the melt content of the AML. Sub-AMLs (SAMLs) shown in light red (*Marjanović et al., 2015*). 1000°C isotherm displaced by the dash line (*Maclennan et al., 2004*). Diagram "A", the MOHO crosses the 1000°C isotherm however it has yet to be faulted. Diagram "B" shows the newly faulted MOHO and reduced percolation of magma to the AML from the mantle causing a build-up of magma and head-pressure at the MOHO. Diagram "C", injection of magma into the MOHO forming a new sill following a decrease in lithostatic pressure.

6.2 Future Work

The next steps in understanding the processes involved in the accretion and development of the MOHO could focus on the following:

(1) *Depth Conversion*. Currently the seismic dataset is displayed in TWT and has not been corrected for velocity variations in the crust. Temperature has a significant effect on the velocity of the seismic waves causing them to slow in areas of higher-temperatures (i.e. the ridge). Lower velocities in turn make structures appear deeper in TWT. Although no velocity model would produce a perfect representation of the EPR geometry, it would provide a better representation of the observed depths of the MOHO than is observed in the TWT model. This could have significant effect on the dip and the depth of the observed structures (e.g. OLRs, terraces).

(2) *The placement of a long-term seismic array on the seafloor at the EPR*. The placement of a broadband ocean bottom seismometer array focused on recording small and deep tectonic tremors in the lower crust for an extended period of time has the potential to outline the areas that are currently deforming. Such data could be used to determine if there is a correlation between the locations of seismic activity in the lower crust and the formation of the terraces and injection of the sills.

(3) *Compare location of terraces and sills with locations of grabens at the seafloor*. When the sills are injected into the lower crust, the crust is displaced vertically. Although the magnitude of the displacement would be small, it may extend to the seafloor forming horst and graben structures. By comparing the location of grabens at the seafloor to the extent of the sills in the lower crust, it would be possible to determine whether the displacement of the lower crust extends to the seafloor. This may be done by overlaying the picked horizons of the sills on top of a topographic image of the seafloor.

(4) *Correlate age of crust to Milancović cycles.* It is possible that the periodic terracing of the MOHO and injection of sills is influenced by the 40 ka Milancović cycle. In the survey area the crust extends on average ~12 km on the western side and ~14 km on the eastern side of the ridge with maximum crustal ages of ~216 ka and 259 ka, respectively. On average 6 terraces are observed on the western side and 7 on the eastern side of the ridge indicating that a new terrace is formed about once every ~37 ka, roughly coinciding with length of the 40 ka Milancović cycle. More work is required to identify whether these cycles actually coincide; however, a 40 ka cycle of sea level rise and fall between glacial cycles would result in fluctuations of the pressure exerted by the ocean on the crust. The increase in pressure from sea level rise could cause magma to build up at the MOHO, increasing the magmatic head pressure. Later, when the sea level drops, the magma is injected into lower crust. This theory may be tested by comparing the outline of the terraces and sills to bathymetry and crustal thickness data collected at the ridge. Initial analyses of bathymetry and crustal thickness data for the EPR from 3D MCS by Boulahanis et al [*2017*] has revealed spectral peaks at Milancović frequencies of 1/100 ka^{-1} and 1/40 ka^{-1} further suggesting a link between Milancović cycles and increased magmatism at MORs.

References

Aghaei, O. 2013. The east pacific rise crustal thickness, MOHO transition zone character and off-axis magma lens melt content from 9°37.5'N to 9°57'N: results from three-dimensional multichannel seismic data analysis. Ph.D. thesis, Department of Earth Sciences, Dalhousie University, Halifax, N.S. http://dalspace.library.dal.ca/handle/10222/40065.

Aghaei, O., Nedimovic, M.R., Carton, H., Carbotte, S.M., Canales, J.P., & Mutter, J.C. 2014. Crustal thickness and moho character of the fast-spreading east pacific rise from 9 degrees 42'N to 9 degrees 57'N from poststack-migrated 3-D MCS data. *Geochemistry, Geophysics, Geosystems - G3, 15* (3): 634-657, http://dx.doi.org.ezproxy.library.dal.ca/10.1002/2013GC005069.

Barth, G.A., and J.C. Mutter. 1996. Variability in oceanic crustal thickness and structure: Multichannel seismic reflection results from the northern East Pacific Rise. *Journal of Geophysical Research,* 101: 17951–17975, doi: 10.1029/96JB00814.

Rioux, M., Lissenberg, C.J., McLean, N.M., Bowring, S.A., MacLeod, C.J., Hellebrand, E., and Shimizu, N. 2012. Protracted timescales of lower crustal growth at the fast-spreading East Pacific Rise. *Nature Geoscience*, 5: 275-278, doi: 10.1038/ngeo1378.

Boudier, F., Nicolas, A., and Ildefonse, B. 1996. Magma chambers in the Oman ophiolite: Fed from the top and the bottom. *Earth Planet. Science Lett*er, 144: 239–250.

Boudier, F., and Nicolas, A. 2011. Axial melt lenses at oceanic ridges-A case study in the Oman ophiolite. *Earth Planet Science Letters*, 304: 313–325.

Boulahanis, B., Langmuir, C.H., Aghaei, O., Nedimovic, M.R., Carbotte, S.M., Carton, H.D., Huybers, P.J., and Canales, J.P. 2017. PP13E-04: Mid-Ocean Ridge Melt Supply and Glacial Cycles: A 3D EPR Study of Crustal Thickness, Layer 2A, and Bathymetry. *2017 AGU Fall Meeting*. 344-345.

Calvert, J.A. 1995. Seismic evidence for a magma chamber beneath the slow-spreading Mid-Atlantic Ridge. *Nature,* 377 : 410-414.

Canales, J. P., Carton, H., Carbotte, S.M., Mutter, J.C., Nedimović, M.R., Xu, M., Aghaei, O., Marjanović, M., and Newman, K.. 2012. Network of off-axis melt bodies at the East Pacific Rise. *Natural Geoscience*, 5: 279–283, doi.org/10.1038/ NGEO1377.

Cann J. R. A Model for Oceanic Crystal Structure Developed. *Geophysical Journal International,* 39 (1): 169–187, doi.org/10.1111/j.1365-246X.1974.tb05446.x.

Carbotte, S., and Macdonald, K. 1992. East Pacific Rise 8°–10°30'N: Evolution of ridge segments and discontinuities from SeaMARC II and three-dimensional magnetic studies. *Journal of Geophysical Research,* 97: 6959–6982, doi: 10.1029/91JB03065.

Chen, Y.J., and Phipps Morgan, J. 1996. The effects of spreading rate, the magma budget, and the geometry of magma emplacement on the axial heat flux at mid-ocean ridges, *Journal of Geophysical Research*, 101: 11475–11482.

Christensen, N.I., and Salisbury, M.H. 1975. Structure and constitution of the lower oceanic crust. *Review of Geophysics and Space Physics*. 13 (1): 57-86.

Collins, J.A., Brocher, T.M., and Karson J.A. 1986. Two-dimensional seismic reflection modeling of the inferred crust-mantle transition in the Bay of Islands Ophiolite. *Journal of Geophysical Research,* 91: 12520–12538.

Crowley, J.W., Kats, R.F., Huybers, P., Langmuir, C.H., and Park, S.H. 2015. Glacial cycles drive variations in the production of oceanic crust. *Science*, 347 (6227): 1237-1240, doi.org.ezproxy.library.dal.ca/10.1126/science.1261508.

Dunn, R. A., Toomey, D.R., and Solomon, S.C. 2000. Three-dimensional seismic structure and physical properties of the crust and shallow mantle beneath the East Pacific Rise at 9°30'N. *Journal of Geophysical Research,* 105 : 23,537–23,55, doi: 10.1029/2000JB900210.

Detrick, R.S., Buhl P., Vera E., Mutter J., Orcutt, J., Madsen, J., and Brocher, T. 1987. Multi-channel seismic imaging of a crustal magma chamber along the East Pacific Rise. *Nature*, 326: 35–41.

Detrick, R.S., Mutter, J.C., Buhl, P., and Kim, I.I. 1990. No evidence from multichannel reflection data for a crustal magma chamber in the *MARK* area on the Mid-Atlantic Ridge. *Nature,* 347: 61-64.

Faure, G., & Mensing, T.M. 2005. Isotopes; principles and applications. John Wiley & Sons, Hoboken, NJ.

Herron, T.J., Stoffa, P.L., and Buhl, P. 1980. Magma chamber and mantle reflections – East Pacific Rise. *Geophysics Research Letters*, 7 (1): 989-992, doi.org/10.1029/GL007i011p00989.

Houtz, R., & Ewing, J. 1976. Upper crustal structure as a function of plate age. *Journal of Geophysical Research*, 81 (14): 2131-2153.

Jousselin, D. and Nicolas, A., 2000. The MOHO transition zone in the Oman ophiolite. Relation with wehrlites in the crust and dunites in the mantle. *Marine Geophysics Research*, 21: 229–241.

Karson, J.A., Collins, J.A., and Casey, J.F. 1984. Geologic and seismic velocity structure of the crust/mantle transition in the Bay of Islands ophiolite complex, *Journal of Geophysical Research*, 89, 6126–6138, doi: 10.1029/JB089iB07p06126.

Kelemen, P.B., and Aharonov, E. 1998. Periodic formation of magma fractures and generation of layered gabbros in the lower crust beneath oceanic spreading ridges, in Faulting and Magmatism at Mid-Ocean Ridges. *Geophysical Monograph. Series*, 106: 267–289.

Kent, G.M., Harding A.J., and Orcutt J.A. 1993. Distribution of magma beneath the East Pacific Rise between the Clipperton transform and the 9˚17'N deval from forward modeling of common depth point data. *Journal of Geophysical Research*, 98: 13,945–13,969.

Kent, G.M., Harding, A.J., Orcutt, J.A., Detrick, R.S., Mutter, J.C., and Buhl, P. 1994. Uniform accretion of oceanic crust south of the Garrett transform at 14˚15'S on the East Pacific Rise. *Journal of Geophysical Research*, 99: 9097-9116, doi: 10.1029/93JB02872.

Macdonald, K.C., Fox, P.J., Alexander, R.T., Pockalny, R., and Pascal, G. 1996. Volcanic growth faults and the origin of Pacific abyssal hills. *Nature*, 380: 125-129, doi: 10.1038/380125a0.

Macdonald, K.C., Fox, P.J., Miller, S.P., Carbotte, S.M., Edwards, M.H., Eisen, M.F, Fornari, D.J., Perram, L.J., Pockalny, R., Haymon, R.M., Scheirer, D.S., Tighe, S., Weiland, C., and Wilson, D. 1992. The East Pacific Rise and its flanks 8°–18°N: History of segmentation, propagation and spreading direction based on SeaMARC II and SeaBeam studies. *Marine Geophysical Res*earch, 14: 299–344.

Maclennan, J., Hulme, T., & Singh, S. C. (2004). Thermal models of oceanic crustal accretion; linking geophysical, geological and petrological observations. *Geochemistry, Geophysics, Geosystems - G3,* 5 (2), http://dx.doi.org.ezproxy.library.dal.ca/10.1029/2003GC000605.

Marjanović, M., Carton, H., Carbotte, S.M., Nedimović, M.R., Mutter, J.C., and Canales, J.P. 2015. Distribution of melt along the East Pacific Rise from 9°30’ to 10°N from an amplitude variation with angle of incidence (AVA) technique. *Geophysics Journal International*, 203, 1–21, doi:10.1093/gji/ggv251.

Nchsbands. 2017. [online] Available from: https://encrypted-tbn0.gstatic.com/images?q=tbn:ANd9GcQAqNr3m36I6JUliSv4V3oyeJnO7N8qsEXh6toU7VdoAvZ1sI6I. [cited 10 April 2018].

Nedimović, M.R., Carbotte, S.M., Harding, A.J., Detrick, R.S., Canales, J.P., Diebold, J.B., Kent, G.M., Tischer, M., and Babcock, J.M. 2005. Frozen magma lenses below the oceanic crust, *Nature*, 436: 1149–1152, doi: 10.1038/nature03944

Nicolas, A. 1989. Structures of ophiolites and dynamics of oceanic lithosphere. Kluwer Academic Publishers, Norwell, Maine, U.S.A.

Nicolas, A., and Boudier, F. 2015. Structural contribution from the Oman ophiolite to processes of crustal accretion at the East Pacific Rise. *Terra Nova*, 27 (2): 77-96, doi: 10.1111/ter.12137.

Orcutt, J., Kennett B., Dorman L., and Prothero, W. 1975. Evidence of Low Velocity Zone Underlying a Fast-Spreading Rise Crest. *Nature*, 256: 475-476.

Pallister, J.S. And Hopson, C.A. 1981. Samail ophiolite plutonic suite, field relations, phase variation, cryptic variation and layering, and a model of a spreading ridge magma chamber. *Journal of Geophysical Research*, 86: 2593-2644.

Schouten, H., and C. Denham. 1995. Virtual ocean crust. *Eos Transactions of the American Geophysical Union,* 76 (Spring meet): 84.

Singh, S.C., Harding, A.J., Kent, G.M., Sinha, M.C., Combier, V., Bazin, S., Tong, C.H., Pye, J.W., Barton, P.J., Hobbs, R.W., White, R.S., and Orcutt, J.A. 2006. Seismic reflection images of the Moho underlying melt sills at the East Pacific Rise. *Nature,* 442: 287–290.

Sinton, J. M., & Detrick, R. S. 1992. Mid-ocean ridge magma chambers. Journal of Geophysical Research: Solid Earth, 97 (B1), doi: 10.1029/91JB02508.

Spudich, P. and Orcutt, J. 1980. Petrology and porosity of an oceanic crustal site: Results from wave form modeling of seismic refraction data. Journal of Geophysical Research: Solid Earth, 85 (B3): 0148-0227, doi: 10.1029/JB085iB03p01409.

Sykes, L.R. 1967. Mechanism of earthquakes and nature of faulting on the mid-oceanic ridges. *Journal of Geophysical Research.* 72 (8), 2131-2153, doi:http://dx.doi.org.ezproxy.library.dal.ca/10.1029/JA072i008p02131

Toomey, D.R., Purdy G.M., Solomon S.C., and Wilcock, W.S.D. 1990. The three-dimensional seismic velocity structure of the East Pacific Rise near latitude 9°30'N. Nature, 347: 639–645, doi: 10.1038/347639a0.

Toomey, D.R., Jousselin, D., Dunn, R.A., Wilcock, W.S.D. and Detrick, R.S. 2007. Skew of mantle upwelling beneath the East Pacific Rise governs segmentation. *Nature,* 446 : 409–414.

Vera, E.E., Mutter J.C., Buhl, P., Orcutt, J.A., Harding, A.J., Kappus, M.E., Detrick R.S., and Brocher, T.M. 1990. The structure of 0- to 0.2-m.y.-old oceanic crust at 9°N on the East Pacific Rise from expanded spread profiles. Journal of Geophysical Research, 95: 15529–15556.

Appendix A

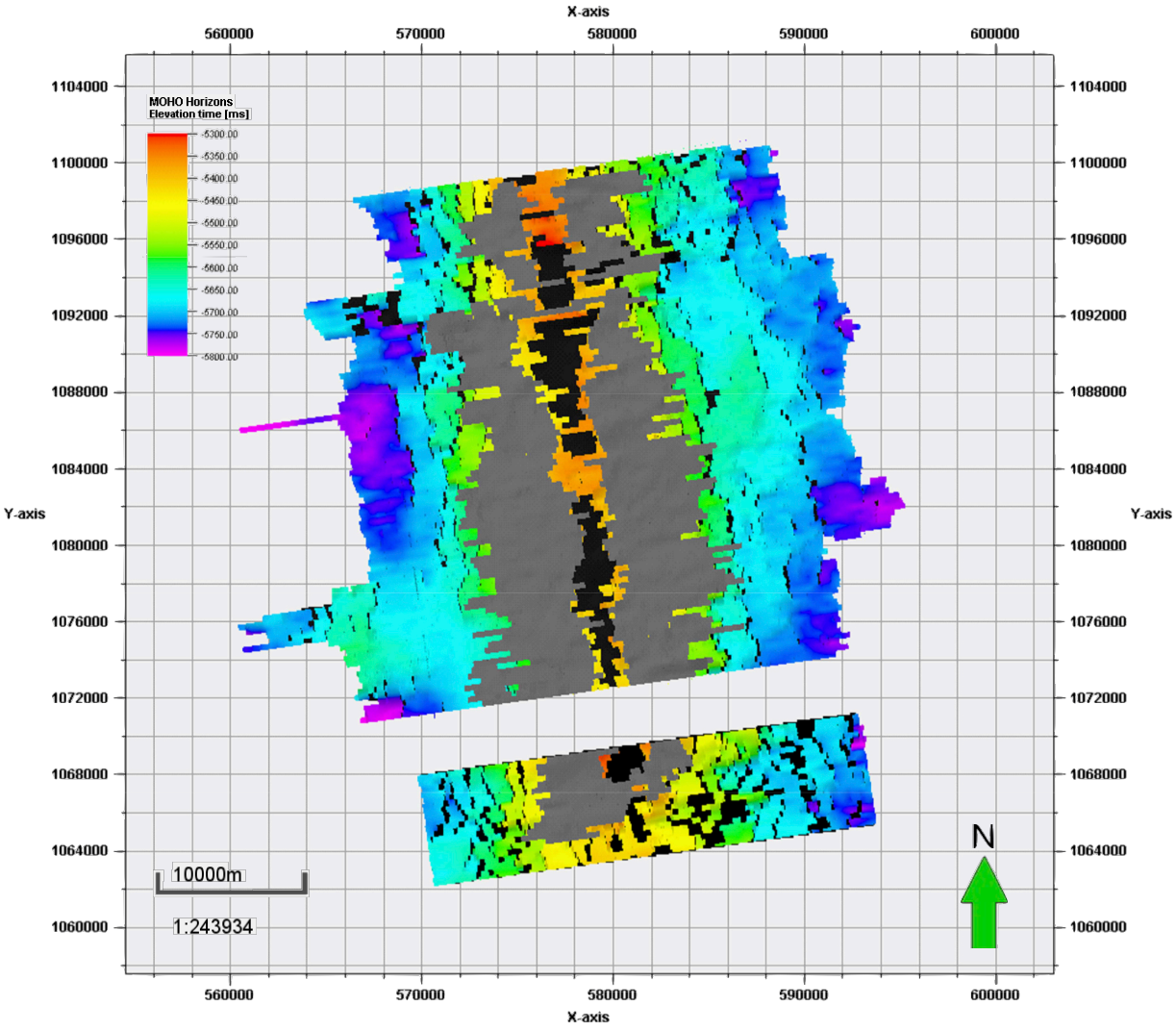

Figure A.1 OLR 0 (grey) originating within 1 km from the ridge axis and observed extending over the top terrace (T1). Displayed on top of the reflection MOHO horizon (Figure 4.9). Colour scale indicates TWT; black background added to increase contrast for areas where reflection MOHO was not possible to pick. Both axes are distance in meters with original latitudes and longitudes converted to UTM using geodetic reference frame WGS84 and zone 13N.

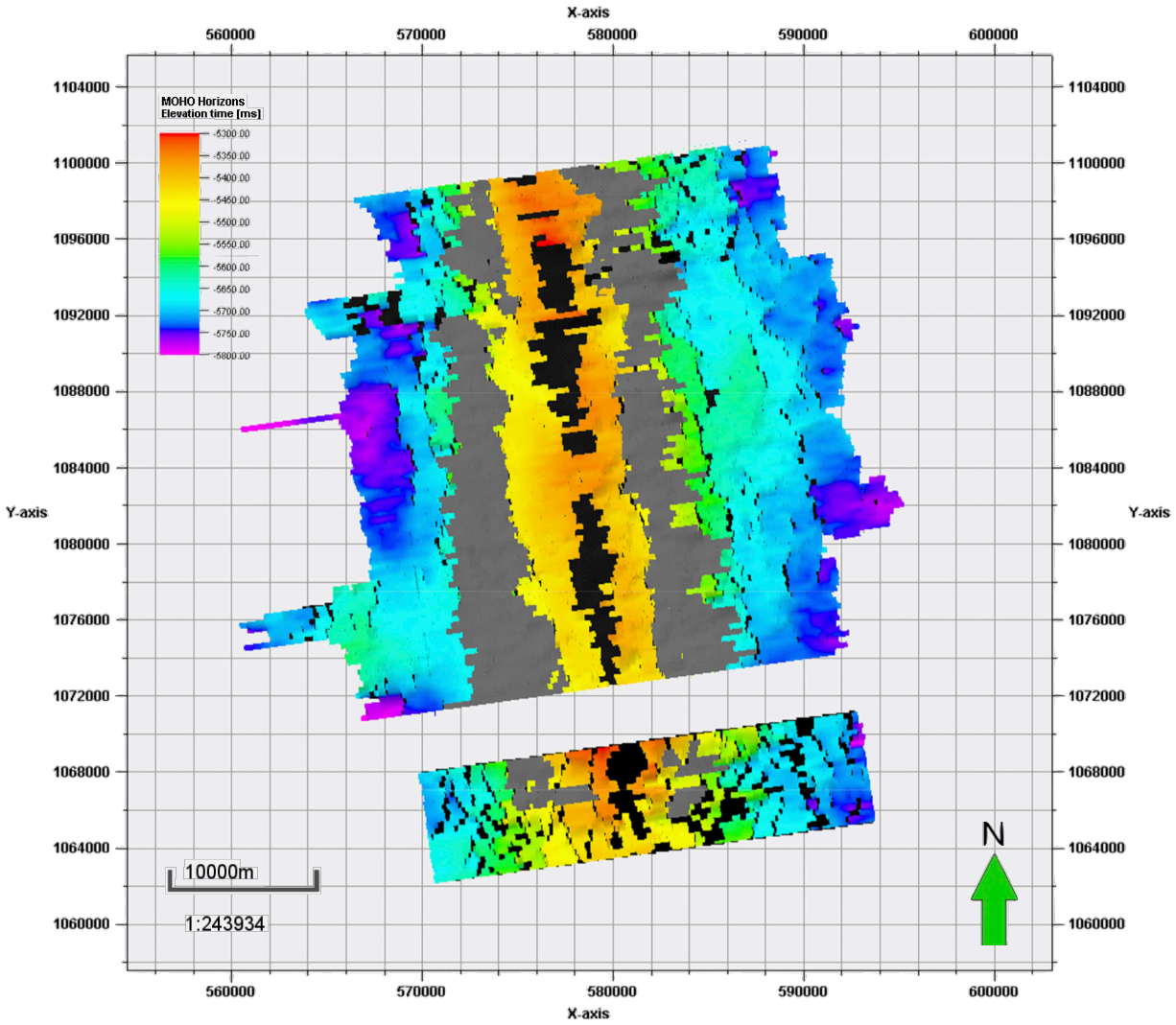

Figure A.2 OLR 1 (grey) off lapping from the top terrace (T1) on either side of the ridge, displayed on top of the reflection MOHO horizon (Figure 4.9). Colour scale indicates TWT; black background added to increase contrast for areas where reflection MOHO was not possible to pick. Both axes are distance in meters with original latitudes and longitudes converted to UTM using geodetic reference frame WGS84 and zone 13N.

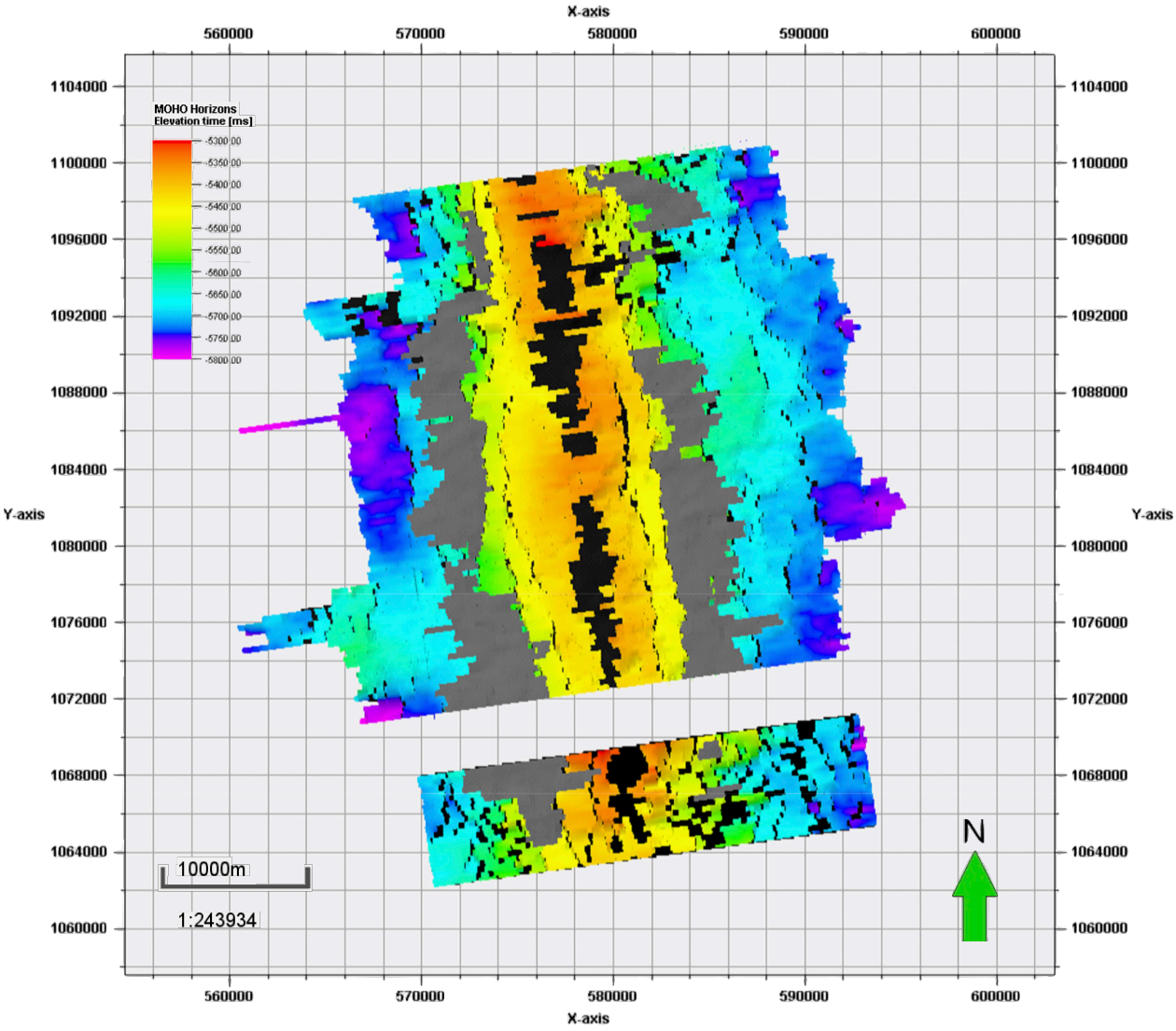

Figure A.3 OLR 2 (grey) off lapping from the top terrace (T2) on either side of the ridge, displayed on top of the reflection MOHO horizon (Figure 4.9). Colour scale indicates TWT; black background added to increase contrast for areas where reflection MOHO was not possible to pick. Both axes are distance in meters with original latitudes and longitudes converted to UTM using geodetic reference frame WGS84 and zone 13N.

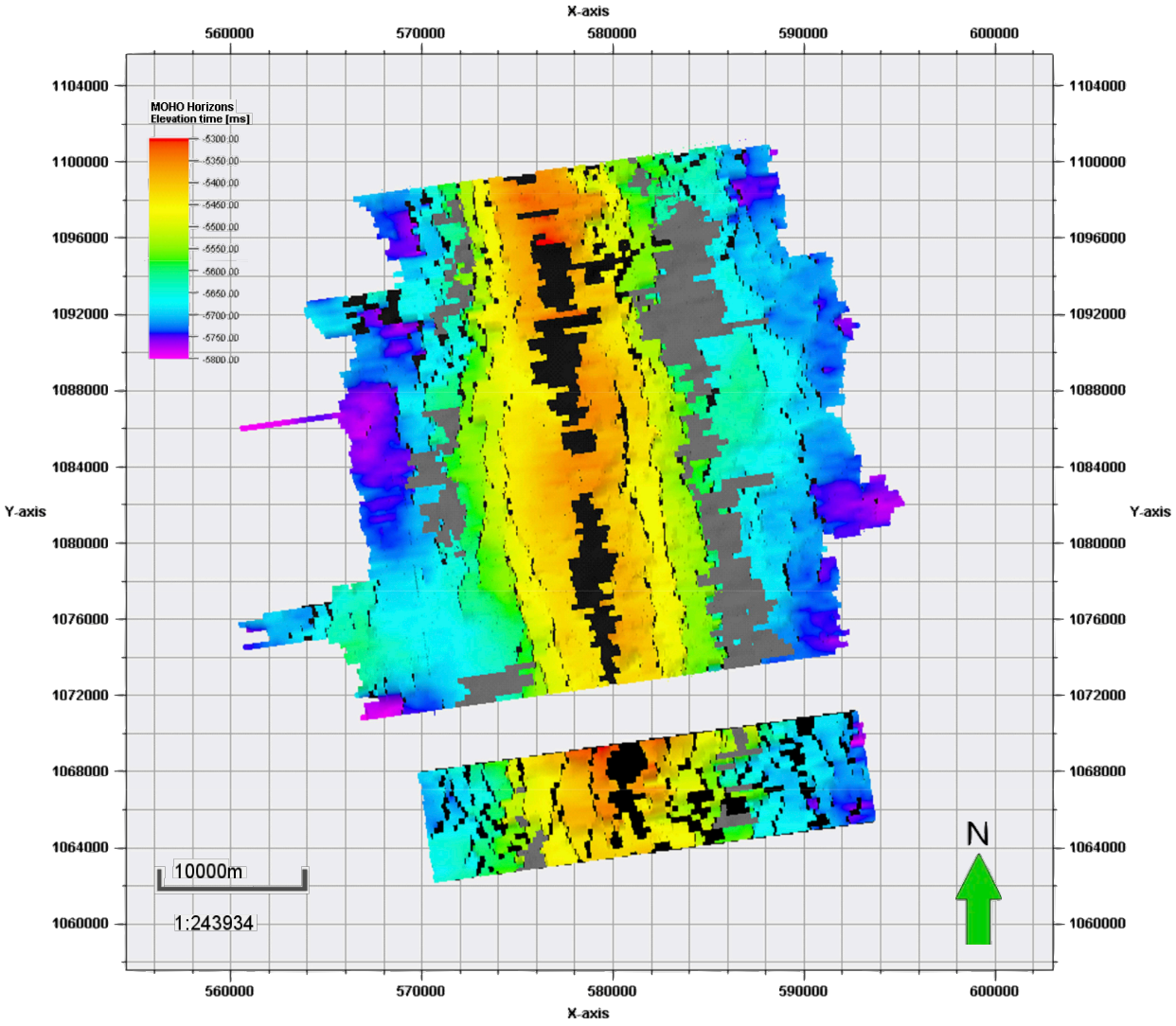

Figure A.4 OLR 3 (grey) off lapping from the top terrace (T3) on either side of the ridge, displayed on top of the reflection MOHO horizon (Figure 4.9). Colour scale indicates TWT; black background added to increase contrast for areas where reflection MOHO was not possible to pick. Both axes are distance in meters with original latitudes and longitudes converted to UTM using geodetic reference frame WGS84 and zone 13N.

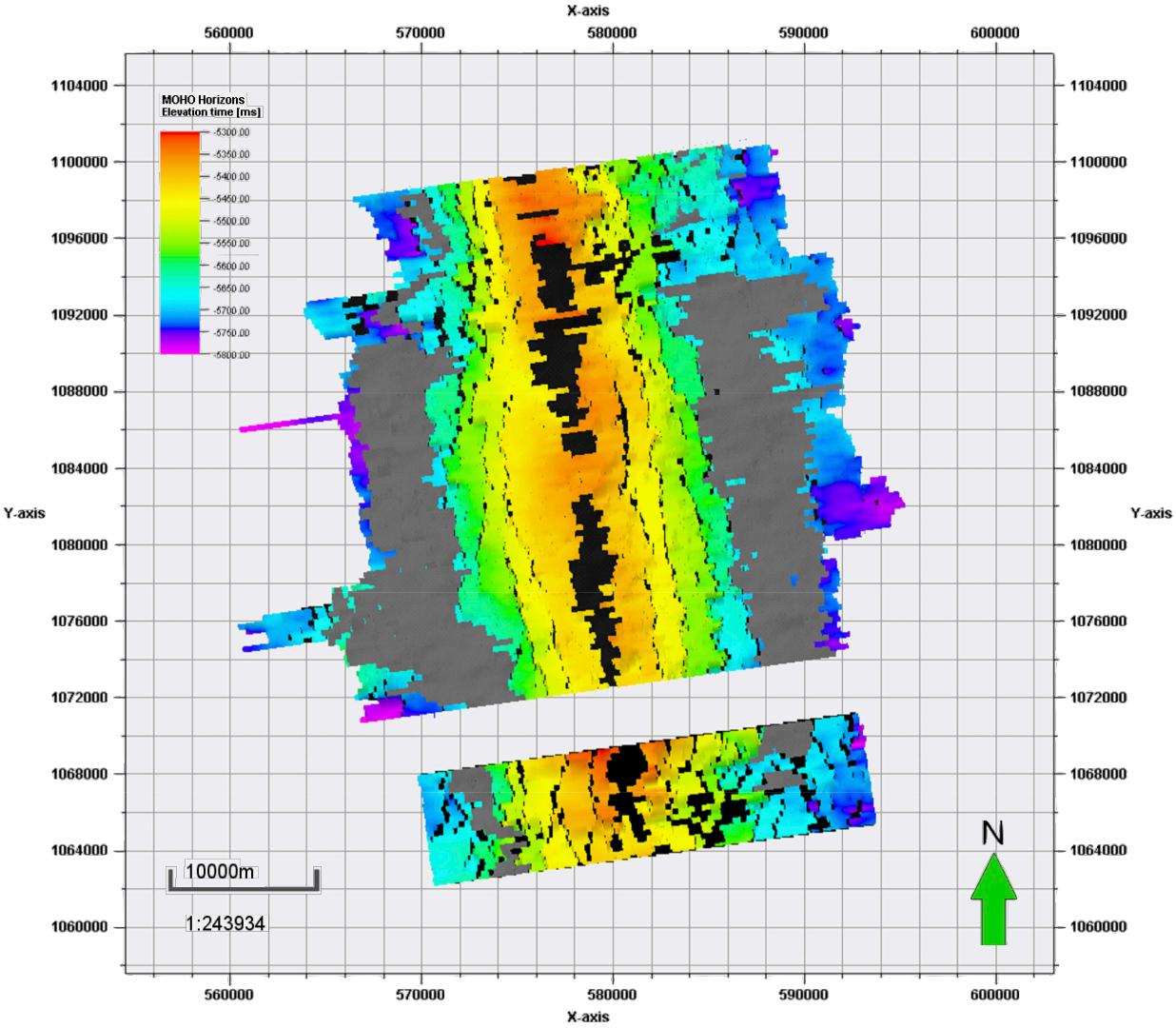

Figure A.5 OLR 4 (grey) off lapping from the top terrace (T4) on either side of the ridge, displayed on top of the reflection MOHO horizon (Figure 4.9). Colour scale indicates TWT; black background added to increase contrast for areas where reflection MOHO was not possible to pick. Both axes are distance in meters with original latitudes and longitudes converted to UTM using geodetic reference frame WGS84 and zone 13N.

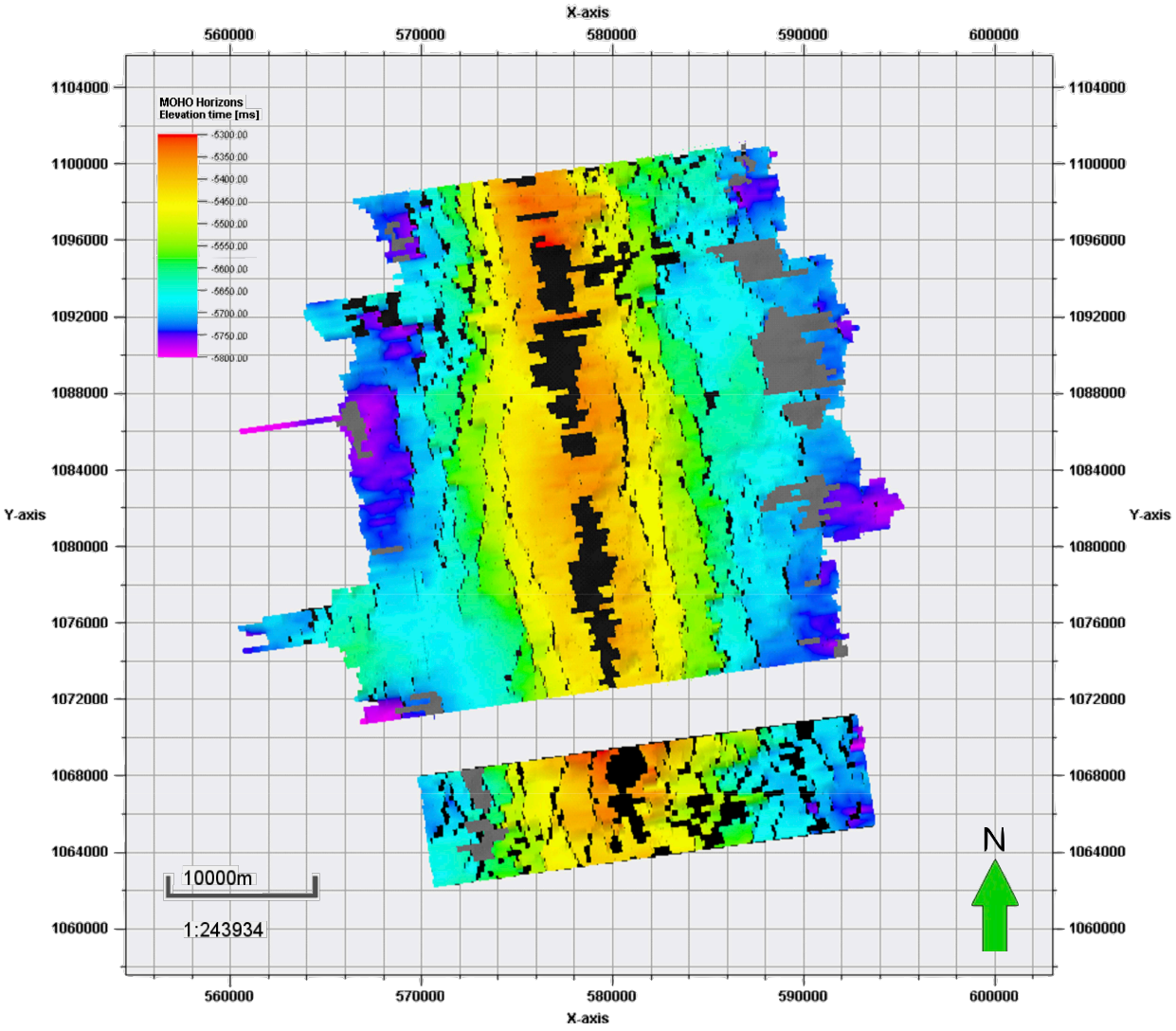

Figure A.6 OLR 5 (grey) off lapping from the top terrace (T5) on either side of the ridge, displayed on top of the reflection MOHO horizon (Figure 4.9). Colour scale indicates TWT; black background added to increase contrast for areas where reflection MOHO was not possible to pick. Both axes are distance in meters with original latitudes and longitudes converted to UTM using geodetic reference frame WGS84 and zone 13N.

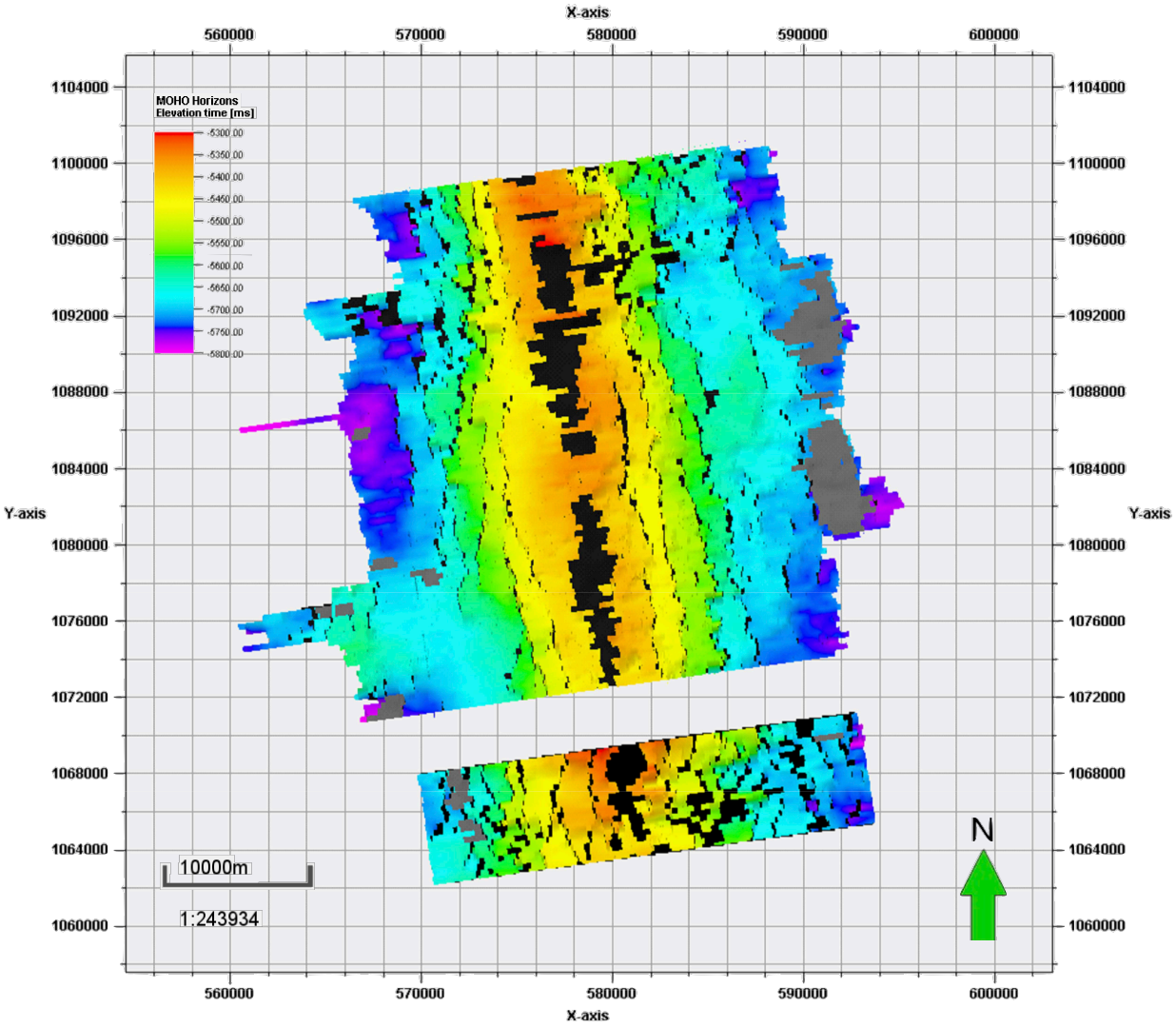

Figure A.7 OLR 6 (grey) off lapping from the top terrace (T6) on either side of the ridge, displayed on top of the reflection MOHO horizon (Figure 4.9). Colour scale indicates TWT; black background added to increase contrast for areas where reflection MOHO was not possible to pick. Both axes are distance in meters with original latitudes and longitudes converted to UTM using geodetic reference frame WGS84 and zone 13N.

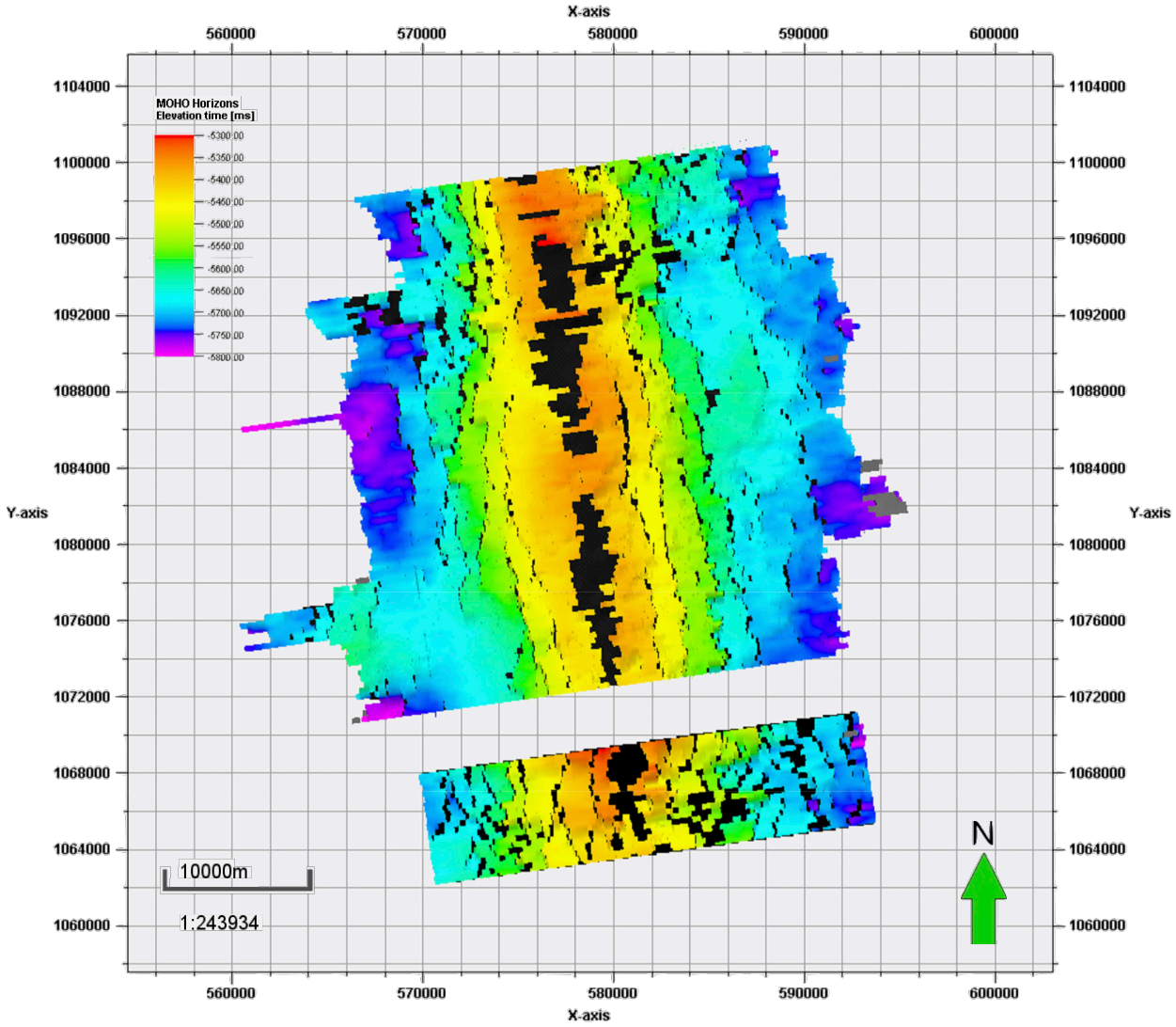

Figure A.8 OLR 7 (grey) off lapping from the top terrace (T7) on either side of the ridge, displayed on top of the reflection MOHO horizon (Figure 4.9). Colour scale indicates TWT; black background added to increase contrast for areas where reflection MOHO was not possible to pick. Both axes are distance in meters with original latitudes and longitudes converted to UTM using geodetic reference frame WGS84 and zone 13N.